Journal of Non-Newtonian Fluid Mechanics 291 (2021) 104514

Contents lists available at ScienceDirect

Journal of Non-Newtonian Fluid Mechanics

journal homepage: www.elsevier.com/locate/jnnfm

Localized stress amplification in inertialess channel flows of viscoelastic fluids

Gokul Hariharan [a], Mihailo R. Jovanović [b], Satish Kumar [a,*]

[a] Department of Chemical Engineering and Materials Science, University of Minnesota, Minneapolis, MN 55455, USA
[b] Ming Hsieh Department of Electrical and Computer Engineering, University of Southern California, Los Angeles, CA 90089, USA

ABSTRACT

Nonmodal analysis typically uses square-integrated quantities to characterize amplification of disturbances. However, such measures may be misleading in viscoelastic fluids, where polymer stresses can be strongly amplified over a small region. Here, we show that when using a localized measure of disturbance amplification, spanwise-constant polymer-stress fluctuations can be more amplified than streamwise-constant polymer-stress fluctuations, which is the opposite of what is observed when a square-integrated measure of disturbance amplification is used. To demonstrate this, we consider a model problem involving two-dimensional pressure-driven inertialess channel flow of an Oldroyd-B fluid subject to a localized time-periodic body force. Nonmodal analysis of the linearized governing equations is performed using recently developed well-conditioned spectral methods that are suitable for resolving sharp stress gradients. It is found that polymer-stress fluctuations can be amplified by an order of magnitude while there is only negligible amplification of velocity fluctuations. The large stress amplification arises from the continuous spectrum of the linearized problem, and may put the flow into a regime where nonlinear terms are no longer negligible, thereby triggering a transition to elastic turbulence. The results suggest an alternate mechanism that may be useful for understanding recent experimental observations of elastic turbulence in microchannel flows of viscoelastic fluids.

1. Introduction

A Newtonian fluid can transition from laminar to turbulent flow when inertial forces become sufficiently large compared to viscous forces. In contrast, viscoelastic fluids can exhibit turbulent-like flow even when inertial forces are much weaker than viscous forces [1–4]. This turbulent-like flow state (elastic turbulence) arises when elastic forces become sufficiently large relative to viscous forces. Elastic turbulence may be helpful for enhancing transport in flows with weak inertia [5], such as those that arise in drug delivery systems, medical diagnostic devices, and high-heat-flux integrated circuits [6]. However, elasticity-driven instabilities in polymer processing operations like extrusion are detrimental to the quality of final products [7,8]. It is therefore important to understand possible physical mechanisms that could trigger a transition to elastic turbulence.

Flows of viscoelastic fluids with curved streamlines can be linearly unstable in the absence of inertia, and this instability provides a mechanism for initiating the transition to elastic turbulence [1,2]. In contrast, channel flows of viscoelastic fluids with straight streamlines (e.g., plane Poiseuille and Couette flows) are predicted to be linearly stable in the absence of inertia [7,9–11]. However, such flows appear to be unstable to finite-amplitude perturbations, and it has been argued that this provides a mechanism for initiating transition to elastic turbulence [3,4,8]. Nevertheless, the question of how such finite-amplitude perturbations arise remains an open one.

Even if standard modal (i.e., eigenvalue) analysis predicts that a flow is linearly stable, transition to another flow state could be initiated via a linear mechanism if there is nonmodal amplification of disturbances. A sufficiently large disturbance amplification could put the flow into a regime where nonlinear terms are no longer negligible even if modal analysis predicts that the flow is asymptotically stable. The effects of these nonlinear terms could then lead to flow transition. Nonmodal analysis of channel flows of viscoelastic fluids indicates that velocity and polymer-stress fluctuations can undergo considerable amplification even when inertial effects are much weaker than elastic effects, with the largest amplification occurring for streamwise-constant disturbances [12–17].

Disturbance amplification in nonmodal analysis of channel flows is typically measured in terms of quantities that are square-integrated along the channel gap [18–21]. For example, the integral of the square of the magnitude of the velocity fluctuation vector provides a measure of the kinetic energy of the velocity fluctuations [18–20]. The objective of the present paper is to demonstrate that such square-integrated measures may be misleading in viscoelastic fluids, where polymer stresses can be highly localized (e.g., [11,22–25]).

To understand why a square-integrated measure may be misleading for functions that are strongly amplified only in a small region, consider a function [17,26] whose square yields a Gaussian function with a small

* Corresponding author.
E-mail address: kumar030@umn.edu (S. Kumar).

https://doi.org/10.1016/j.jnnfm.2021.104514
Received 17 August 2020; Received in revised form 22 December 2020; Accepted 3 March 2021
Available online 8 March 2021
0377-0257/© 2021 Elsevier B.V. All rights reserved.

standard deviation, α,

$$g^2(y) = \frac{1}{2\sqrt{\pi\alpha}}\, \mathrm{e}^{-\frac{y^2}{4\alpha}}. \tag{1}$$

The Gaussian function (1) has the property that its peak value increases with a decrease in α. For example, when $\alpha = 0.01$, the peak value of the Gaussian is ~ 3, whereas when $\alpha = 0.005$, the peak value is ~ 12.

However, no matter how large the peak value of the Gaussian is, its integral is always of unit magnitude, i.e.,

$$\int_{-\infty}^{\infty} g^2(y)\,\mathrm{d}y \;=\; 1. \tag{2}$$

The square-integrated measure in (2) does not appropriately weight the large magnitude of the Gaussian function over a small region that occurs when α is very small. Similarly, if a polymer-stress fluctuation is amplified by orders of magnitude over a small region, the square-integrated measure typically used in nonmodal analysis will overlook the sheer magnitude of the polymer stress that occurs locally. Yet, such large polymer stresses and the corresponding gradients could put the flow into a regime where nonlinear terms are no longer negligible, and this could lead to a flow transition.

Besides being of fundamental interest, the results of the present paper may also be relevant for understanding experimental observations of elastic turbulence in straight microchannels by Pan et al. and Qin et al. [3,4]. Pressure-driven flow of a polymer solution having nearly constant shear viscosity was observed in a channel of length 3 cm and cross-section $90\,\mu\mathrm{m} \times 100\,\mu\mathrm{m}$. The Reynolds number was ~ 0.01, and an array of cylinders (diameter $\sim 50\,\mu\mathrm{m}$) in the entry region of the channel was used to perturb the flow. Particle tracking velocimetry reveals that the magnitude of centerline velocity fluctuations can initially decrease along the channel length before increasing (inset of Figure 3 in [4]), resulting in a turbulent-like flow far downstream of the cylinders. This occurs when the number of cylinders and the Weissenberg number (ratio of fluid relaxation time to characteristic flow time) are sufficiently large.

Because the magnitude of centerline velocity fluctuations initially decreases along the channel length, it was argued that the transition to elastic turbulence principally involves a nonlinear (finite-amplitude) instability rather than a linear mechanism such as modal or nonmodal growth of disturbances [3]. If a linear mechanism played an important role in the experiments, one might expect velocity fluctuations to initially increase along the channel length, rather then first decreasing before increasing.

However, it is not clear what causes the finite-amplitude perturbation, and one possibility is that it could arise from a linear mechanism that was overlooked in prior work. In particular, if polymer-stress fluctuations are amplified significantly while velocity fluctuations undergo negligible amplification, then the amplified polymer stresses could act as a finite-amplitude perturbation that triggers flow transition even though the velocity fluctuations (which are typically what are measured experimentally) do not appear to be significantly amplified. Although we do not seek here to provide a definitive explanation of the experimental observations of Pan et al. [3] and Qin et al. [4], our results reveal the presence of such an alternate linear mechanism, which involves large amplification of polymer-stress fluctuations over a small region.

To gain insight into the above issues, we consider in this paper a model problem involving pressure-driven inertialess channel flow of an Oldroyd-B fluid subject to a localized time-periodic body force. Our model problem allows us to isolate the effects of elasticity from those of inertia, the finite-extensibility of polymer molecules, and shear-thinning. Time-periodic body forces are examined to be consistent with prior work [16] and because they yield fundamental information about the frequency response of the flow. Since the cylinders in the experiments of Pan et al. [3] and Qin et al. [4] discussed above exert a localized force on the fluid and create a perturbation to the flow that is time-periodic [27], our model problem may also provide some insights into these and related experiments.

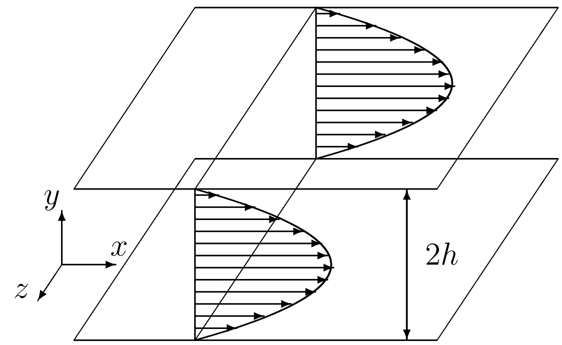

Fig. 1. Flow geometry and the steady-state velocity profile for plane Poiseuille flow.

One of the key findings of the present paper is that if a localized measure of disturbance amplification is used, then spanwise-constant polymer-stress fluctuations can be more amplified than streamwise-constant polymer-stress fluctuations. This is the opposite of what is observed if a square-integrated measure of disturbance amplification is used. Moreover, it is found that when using a localized measure, stress fluctuations can be amplified by an order of magnitude over a small region in spanwise-constant (i.e., two-dimensional) flows whereas amplification of velocity fluctuations is negligible. The issue of whether streamwise-constant disturbances, spanwise-constant disturbances, or some other scenario is principally responsible for transition to elastic turbulence can only be settled by nonlinear calculations. Nevertheless, the present work highlights the potential importance of localized amplification of spanwise-constant stress fluctuations, a mechanism unique to viscoelastic fluids and one that was overlooked in prior work that emphasized the use of square-integrated measures of disturbance amplification [12–17].

Our paper is organized as follows. In Section 2 we present the problem formulation, and in Section 3 we discuss the numerical methods used. In Section 4 we compare localized and square-integrated measures of stress amplification. In Section 5 we identify the role played by the continuous spectrum of the linearized problem in stress amplification. We summarize our findings in Section 6, and relegate technical details to the appendices.

2. Problem formulation

2.1. Governing equations

We consider inertialess pressure-driven flow of an Oldroyd-B fluid between two parallel planes separated by a distance $2h$ (Fig. 1). We scale length with h, velocity with the maximum magnitude of the steady-state velocity U_0, and time with h/U_0. Pressure is scaled with $\mu_T U_0/h$, where μ_T is the effective shear viscosity of the fluid, and polymer stresses with $\mu_p U_0/h$, where $\mu_p = \mu_T - \mu_s$ and μ_s is the solvent viscosity.

Two nondimensional groups result from this scaling that characterize the material properties of the fluid. The viscosity ratio, $\beta = \mu_s/\mu_T$, gives the ratio of the solvent to the total viscosity. The Weissenberg number $We = \lambda_p U_0/h$, gives the ratio of the fluid relaxation time λ_p to the characteristic flow time h/U_0.

The equations governing momentum and mass conservation are [28, 29]

$$-\boldsymbol{\nabla} P \,+\, \beta\,\nabla^2 \boldsymbol{V} \,+\, (1-\beta)\,\boldsymbol{\nabla}\cdot\boldsymbol{T} \,+\, \boldsymbol{D} \;=0, \tag{3a}$$

$$\boldsymbol{\nabla}\cdot\boldsymbol{V} \;=0, \tag{3b}$$

where $\boldsymbol{V} = [\,U \;\; V \;\; W\,]^T$ is the velocity vector, $\boldsymbol{T}$ is the polymer-stress tensor, P is the pressure, and $\boldsymbol{D}$ is the body force. The Oldroyd-B constitutive equation governs the polymer stress,

$$\partial_t \boldsymbol{T} + \boldsymbol{V}\cdot\nabla\boldsymbol{T} - \boldsymbol{T}\cdot\nabla\boldsymbol{V} - (\boldsymbol{T}\cdot\nabla\boldsymbol{V})^T \;=\; -\frac{1}{We}\boldsymbol{T} + \frac{1}{We}\left(\nabla\boldsymbol{V} + \nabla\boldsymbol{V}^T\right). \quad (3c)$$

The steady-state velocity and nonzero components of the polymer stress are given by,

$$\bar{\boldsymbol{V}} \;=\; [\,\bar{U}(y)\;\;0\;\;0\,]^T, \qquad \bar{T}_{xx} \;=\; 2\,We\,\bar{U}'(y)^2, \qquad \bar{T}_{xy} \;=\; \bar{T}_{yx} \;=\; \bar{U}'(y), \quad (4)$$

where $\bar{U}(y) = 1 - y^2$ for plane Poiseuille flow (Fig. 1), and the prime refers to a derivative with respect to y. We consider the dynamics of fluctuations about the steady-state (4) using a standard decomposition in (3), $\boldsymbol{V} = \bar{\boldsymbol{V}} + \boldsymbol{v}$, $\boldsymbol{T} = \bar{\boldsymbol{T}} + \boldsymbol{\tau}$, $P = \bar{P} + p$, and $\boldsymbol{D} = \bar{\boldsymbol{D}} + \boldsymbol{d}$, where $\boldsymbol{v}$, $\boldsymbol{\tau}$, p and $\boldsymbol{d}$ are fluctuations of the velocity, polymer stress, pressure and body force, respectively.

Retaining terms that are linear in the fluctuations leads to the linearized governing equations,

$$-\nabla p + \beta\,\nabla^2\boldsymbol{v} + (1-\beta)\,\nabla\cdot\boldsymbol{\tau} + \boldsymbol{d} \;=\; 0, \quad (5a)$$

$$\nabla\cdot\boldsymbol{v} \;=\; 0, \quad (5b)$$

$$-\frac{1}{We}\boldsymbol{\tau} + \frac{1}{We}\left(\nabla\boldsymbol{v} + \nabla\boldsymbol{v}^T\right) \;=\; \partial_t\boldsymbol{\tau} + \bar{\boldsymbol{V}}\cdot\nabla\boldsymbol{\tau} + \boldsymbol{v}\cdot\nabla\bar{\boldsymbol{T}} - \bar{\boldsymbol{T}}\cdot\nabla\boldsymbol{v} - \boldsymbol{\tau}\cdot\nabla\bar{\boldsymbol{V}} - (\bar{\boldsymbol{T}}\cdot\nabla\boldsymbol{v})^T - (\boldsymbol{\tau}\cdot\nabla\bar{\boldsymbol{V}})^T. \quad (5c)$$

The boundary conditions come from no-slip and no-penetration of the velocity at the channel walls,

$$\boldsymbol{v}(\pm 1) \;=\; 0. \quad (5d)$$

We consider the effects of a persistent body force $\boldsymbol{d}$ of the form

$$\boldsymbol{d}(x,y,z,t) \;=\; \boldsymbol{d}(y)\,\delta(x)\,\delta(z)\,\mathrm{e}^{i\,\omega\,t}, \quad (5e)$$

where $\delta(\cdot)$ is the Dirac delta function, i is the imaginary unit, and ω is the temporal frequency. For simplicity, we now use the symbol $\boldsymbol{d}$ to denote the y-dependence of the body force. The body force in (5e) is localized in the x- and z-directions and is harmonic in time. As we will see in Section 4 (Figs. 5c and 5d), $\boldsymbol{d}(y)$, which emerges from our analysis, is nearly localized at specific points in the y-direction as well.

2.2. Input–output form of governing equations

The linearized governing equations can be put into a form that relates input and output variables. This is accomplished by first applying a Fourier transform to (5) in the x- and z-directions. Since the resultant stress and velocity fields must have the same temporal frequency ω [21] as the body force in (5e), we substitute $\boldsymbol{v}(\boldsymbol{\kappa},y,t) = \boldsymbol{v}(\boldsymbol{\kappa},y)\,\mathrm{e}^{i\,\omega\,t}$, $\boldsymbol{\tau}(\boldsymbol{\kappa},y,t) = \boldsymbol{\tau}(\boldsymbol{\kappa},y)\,\mathrm{e}^{i\,\omega\,t}$, and $p(\boldsymbol{\kappa},y,t) = p(\boldsymbol{\kappa},y)\,\mathrm{e}^{i\,\omega\,t}$ into (5). Here $\boldsymbol{\kappa} = (k_x, k_z)$ is the vector of Fourier modes corresponding to the x- and z-directions. We now use the symbols $\boldsymbol{v}$, $\boldsymbol{\tau}$, and p to denote the amplitude functions, and for convenience we simply refer to them as the velocity, stress, and pressure from now on.

The transformed version of (5c) can be used to express the stress in terms of the velocity. Using that expression to eliminate the stress in the momentum conservation equations (5a) leads to a representation of (5) given by

$$[\mathcal{A}(\boldsymbol{\kappa},\omega,\beta,We)\,\boldsymbol{\phi}(\cdot)](y) \;=\; [\mathcal{B}(\boldsymbol{\kappa})\,\boldsymbol{d}(\cdot)](y), \quad (6a)$$

$$\boldsymbol{v}(y) \;=\; [\mathcal{C}_{\boldsymbol{v}}(\boldsymbol{\kappa})\,\boldsymbol{\phi}(\cdot)](y), \quad (6b)$$

$$\tau_{xx}(y) \;=\; [\mathcal{C}_{xx}(\boldsymbol{\kappa},\omega,We)\,\boldsymbol{\phi}(\cdot)](y). \quad (6c)$$

The input $\boldsymbol{d}$ is the body force in (5a), and $\boldsymbol{\phi} = [\,u\;\;v\;\;w\;\;p\,]^T$. The output is either the velocity vector (6b), or the component τ_{xx} (6c) of the stress tensor. The quantities $\mathcal{A}$, $\mathcal{B}$, $\mathcal{C}_{\boldsymbol{v}}$, and $\mathcal{C}_{xx}$ in (6) are block matrices of differential operators in $y \in [-1 \;\; 1]$ (Appendix A). Note that we have moved the dependence of the amplitude functions on $\boldsymbol{\kappa}$ into these operators so that $\boldsymbol{v}$, $\boldsymbol{\tau}$, and p now depend only on y. The notation $(\cdot)$ is used to emphasize that $\boldsymbol{d}$ and $\boldsymbol{\phi}$ are functions. We consider the velocity vector as the output in (6b) instead of individual components as this enables us to calculate the maximum value of the kinetic energy of velocity fluctuations (see (12)). We consider the xx-component of the stress in (6c) as we found that it shows the largest amplification compared to other stress components.

System (6) can be further simplified (Chapter 3 of [21]) by eliminating pressure and recasting $\mathcal{A}$, $\mathcal{B}$, $\mathcal{C}_{\boldsymbol{v}}$, and $\mathcal{C}_{xx}$ into a form where $\boldsymbol{\phi} = [\,v\;\;\eta\,]^T$ with $\eta = ik_z u - ik_x w$ being the wall-normal vorticity. We refer to the form in which $\boldsymbol{\phi} = [\,u\;\;v\;\;w\;\;p\,]^T$ as the descriptor form, and the form in which $\boldsymbol{\phi} = [\,v\;\;\eta\,]^T$ as the evolution form. The descriptor form is a larger system that involves four variables (u, v, w, and p), whereas the evolution form involves two variables (v and η). However, a numerical solution (see Section 3) using the descriptor form needs fewer basis functions compared to the evolution form [30]. We perform calculations using both forms to confirm our expressions and results. Expressions for $\mathcal{A}$, $\mathcal{B}$, $\mathcal{C}_{\boldsymbol{v}}$, and $\mathcal{C}_{xx}$ in (6) in both forms are provided in Appendix A.

We note that the same set of equations in (6) results from using a body force that is a sinusoidal function of x and z in all space,

$$\boldsymbol{d}(x,y,z,t) \;=\; \boldsymbol{d}(y)\,\mathrm{e}^{i\,\omega\,t + i\,k_x x + i\,k_z z}. \quad (7a)$$

Substituting $\boldsymbol{v}(x,y,z,t) = \boldsymbol{v}(y)\,\mathrm{e}^{i\,\omega\,t+i\,k_x x+i\,k_z z}$, $\boldsymbol{\tau}(x,y,z,t) = \boldsymbol{\tau}(y)\,\mathrm{e}^{i\,\omega\,t+i\,k_x x+i\,k_z z}$, and $p(x,y,z,t) = p(y)\,\mathrm{e}^{i\,\omega\,t+i\,k_x x+i\,k_z z}$ into (5) yields (6). Therefore, solutions to (6) can be interpreted as resulting from (a) a force that is a sinusoidal function of x and z in all space (7a), or (b) a force that is localized at one point in the x- and z-directions (5e). The localized interpretation may be useful for making connections to experiments [3,4] where fixed objects exert a body force on the fluid that is persistent in time and localized in space.

2.2.1. Modal analysis

The eigensystem of (6) that characterizes modal stability of (5) is given by pairs of (nonzero) eigenvectors $\boldsymbol{\phi}(y)$ and eigenvalues λ, with $\omega = -i\,\lambda$, $\lambda \in \mathbb{C}$ (where $\mathbb{C}$ is the set of complex numbers), for which

$$[\mathcal{A}(\boldsymbol{\kappa},\lambda,\beta,We)\,\boldsymbol{\phi}(\cdot)](y) \;=\; 0. \quad (7b)$$

System (6) is linearly unstable for a given $\{\boldsymbol{\kappa},\beta,We\}$ when $\mathrm{Re}(\lambda) > 0$, where $\mathrm{Re}(\cdot)$ is the real part. Prior works have shown that inertialess Couette flow is linearly stable for all $\{\boldsymbol{\kappa},We\}$ when $\beta = 0$ [9,10]. For all other parameters in inertialess plane Couette and Poiseuille flows, several numerical solutions show that system (6) is linearly stable, although to the best of our knowledge, there are no rigorous proofs for linear stability in the full parameter space of $\{\boldsymbol{\kappa},\beta,We\}$ [7,11].

One known solution to (7b) is the continuous spectrum [9,11,31],

$$\lambda(y) \;=\; -\frac{1}{We} - i\,k_x\,\bar{U}(y), \quad (7c)$$

which has a negative real part $-1/We$ and is hence linearly stable (here, $\bar{U}$ is the steady-state velocity for plane Poiseuille flow (see (4))). The continuous spectrum varies in y according to the continuous function, $\bar{U}(y)$, and reverts to a discrete eigenvalue $\lambda = -1/We$ when $k_x = 0$. As we will see in Section 5, (7c) plays an important role in inducing large stress amplification from small-amplitude body forces.

2.2.2. Nonmodal analysis

While modal analysis is centered around finding solutions to (7b), nonmodal analysis considers the operator [21] $\mathcal{A}^{-1}(\boldsymbol{\kappa},\omega,\beta,We)$ (see (6a)) in conjunction with the input body force ($\boldsymbol{d}$ in (5a)) and a selected velocity or stress output (see (6b) and (6c), respectively). In particular,

$$\boldsymbol{v}(y) \;=\; [\mathcal{T}_{\boldsymbol{v}}(\omega)\,\boldsymbol{d}(\cdot)](y), \quad (8a)$$

$$\tau_{xx}(y) \;=\; [\mathcal{T}_{xx}(\omega)\,\boldsymbol{d}(\cdot)](y), \tag{8b}$$

where $\mathcal{T}_{\boldsymbol{v}}$ and $\mathcal{T}_{xx}$ are the resolvent operators that map the body force ($\boldsymbol{d}$ in (5a)) to the velocity and stress, respectively,

$$\mathcal{T}_{\boldsymbol{v}}(\omega) \;=\; \mathcal{C}_{\boldsymbol{v}}\mathcal{A}^{-1}(\omega)\mathcal{B}, \qquad \mathcal{T}_{xx}(\omega) \;=\; \mathcal{C}_{xx}(\omega)\mathcal{A}^{-1}(\omega)\mathcal{B}. \tag{8c}$$

Note that operators $\mathcal{C}_{\boldsymbol{v}}$, $\mathcal{A}$, $\mathcal{B}$, and $\mathcal{C}_{xx}$ in (8c) were introduced in (6). We suppress the dependence of the operators on $\{\boldsymbol{\kappa}, \beta, We\}$ in (8) for notational convenience.

One measure of the amount of nonmodal amplification in a system is the resolvent norm [21]. We next discuss the resolvent norm of a generic resolvent operator $\mathcal{T}$ corresponding to an output operator $\mathcal{C}$ in (6) that holds for both the velocity ($\mathcal{C}_{v}$ in (6b)) and the stress ($\mathcal{C}_{xx}$ in (6c)) outputs in (8),

$$\mathcal{T}(\omega) \;=\; \mathcal{C}(\omega)\,\mathcal{A}^{-1}(\omega)\,\mathcal{B}. \tag{9}$$

2.3. The resolvent norm

The resolvent norm of operator $\mathcal{T}$ in (9) provides a measure of the maximum value of the square-integrated velocity (6b) (for $\mathcal{T}_{\boldsymbol{v}}$) or the stress (6c) (for $\mathcal{T}_{xx}$),

$$\int_{-1}^{1} \boldsymbol{v}^{\dagger}(y)\boldsymbol{v}(y)\,\mathrm{d}y, \qquad \int_{-1}^{1} \tau_{xx}^{\dagger}(y)\tau_{xx}(y)\,\mathrm{d}y, \tag{10}$$

for any square-integrable body force ($\boldsymbol{d}$ in (5a)) of a unit $L^2[-1\ \ 1]$ norm,

$$\|\boldsymbol{d}\|_2^2 \;:=\; \int_{-1}^{1} \boldsymbol{d}^{\dagger}(y)\boldsymbol{d}(y)\,\mathrm{d}y, \tag{11}$$

where $\|\cdot\|_2$ is the $L^2[-1\ \ 1]$ norm, and $(\cdot)^{\dagger}$ is the adjoint [19,21]. The square-integrated velocity in (10) yields the kinetic energy of velocity fluctuations integrated over $y \in [-1\ \ 1]$,

$$\int_{-1}^{1} \boldsymbol{v}^{\dagger}(y)\boldsymbol{v}(y)\,\mathrm{d}y \;=\; \int_{-1}^{1} |u(y)|^2 + |v(y)|^2 + |w(y)|^2\,\mathrm{d}y. \tag{12}$$

The resolvent norm is given by the principal singular value of $\mathcal{T}$ [21,32], and is formally defined as

$$\max_{\boldsymbol{d}\,\in\,\mathbb{H}^{3\times 1},\ \boldsymbol{d}\neq 0} \frac{\|\mathcal{T}(\omega)\boldsymbol{d}\|_2}{\|\boldsymbol{d}\|_2} \;=\; \sigma_0[\mathcal{T}], \tag{13}$$

where $\mathbb{H}$ is the set of square-integrable functions. The principal singular value σ_0 is computed using a singular value decomposition (SVD) of $\mathcal{T}$, as described in Section 3. We will now discuss quantities obtained from a SVD of $\mathcal{T}$ which are typically used in nonmodal analysis, along with their physical interpretation.

The SVD of $\mathcal{T}_{\boldsymbol{v}}$ in (8a) yields the singular values σ, body forces, and velocities such that [32]

$$\sigma\,\hat{\boldsymbol{v}}(y) \;=\; [\mathcal{T}_{\boldsymbol{v}}(\omega)\,\hat{\boldsymbol{d}}(\cdot)](y). \tag{14}$$

where $\hat{\boldsymbol{v}}$ and $\hat{\boldsymbol{d}}$ are quantities with a unit $L^2[-1\ \ 1]$ norm (11). Expression (14) implies that a body force $\hat{\boldsymbol{d}}$ acting on $\mathcal{T}_{\boldsymbol{v}}$ results in a $\hat{\boldsymbol{v}}$ with an amplification of magnitude σ. Comparing (8a) and (14), the velocity that results from the body force $\hat{\boldsymbol{d}}$ in (14) is given by

$$\boldsymbol{v}(y) \;=\; \sigma\,\hat{\boldsymbol{v}}(y). \tag{15}$$

Taking the $L^2[-1\ \ 1]$ norm (11) of both sides of (15) we have

$$\|\boldsymbol{v}\|_2^2 \;=\; \sigma^2\|\hat{\boldsymbol{v}}\|_2^2 = \sigma^2, \tag{16}$$

where the last equality in (16) holds as $\hat{\boldsymbol{v}}$ has a unit $L^2[-1\ \ 1]$ norm (see (11)). Together, (16), (11), and (12) indicate that the square of the largest (i.e., principal) singular value gives the maximum possible value of the kinetic energy of velocity fluctuations integrated in the y-direction for any square-integrable body force of a unit $L^2[-1\ \ 1]$ norm (For a rigorous proof that the largest singular value is the resolvent norm (13), see [33].)

Similar to (14)–(16), the SVD of $\mathcal{T}_{xx}$ in (8b) yields the singular values σ, body forces, and stresses such that [32],

$$\sigma\,\hat{\tau}_{xx}(y) \;=\; [\mathcal{T}_{xx}(\omega)\,\hat{\boldsymbol{d}}(\cdot)](y), \tag{17}$$

where $\hat{\tau}_{xx}$ is a quantity with a unit $L^2[-1\ \ 1]$ norm. Similar to (15), we have by using (8b) and (17),

$$\tau_{xx}(y) \;=\; \sigma\,\hat{\tau}_{xx}(y), \tag{18}$$

and taking the $L^2[-1\ \ 1]$ norm (11) of both sides of (18) we arrive at

$$\|\tau_{xx}\|_2^2 \;=\; \sigma^2 \tag{19}$$

From (19), (10), and (11), the largest singular value from the SVD of $\mathcal{T}_{xx}$ gives the maximum possible value of the square-integrated stress for any square-integrable body force of unit $L^2[-1\ \ 1]$ norm [32].

2.4. Localized amplification

As noted earlier, nonmodal analysis typically quantifies disturbance amplification in terms of quantities that are square-integrated along the channel width (see (10)). However, such measures overlook quantities that are highly amplified over a small region as discussed in Section 1. In this paper, we quantify localized amplification as follows,

$$\boldsymbol{v}(y^*) \;:=\; |\boldsymbol{v}(y)|_{\max}, \qquad \tau_{xx}(y^*) \;:=\; |\tau_{xx}(y)|_{\max}, \tag{20}$$

where y^* is the location at which the maximum occurs for a given body force. Note that $\boldsymbol{v}(y)$ and $\tau_{xx}(y)$ are calculated using the SVD and (15) and (18).

Prior works on nonmodal analysis [12–16] show that the maximum nonmodal amplification (as given by (10)) occurs when $k_x = 0$ in (6). This corresponds to streamwise-constant disturbances, and system (6) when $k_x = 0$ is frequently referred as the two-dimensional three-component (2D3C) model [13–16,34]. In the present work, we find that localized amplification (as defined in (20)) is more prominent when $k_z = 0$ and the stress, velocity, and body force are restricted to the (x, y)-plane. This corresponds to spanwise-constant disturbances, and will be referred to as the 2D model. We consider here only these two models and not a full 3D model owing to numerical limitations (see Chapter 3 of [35]).

3. Numerical methods

The SVD of $\mathcal{T}$ in (9) is determined by using an eigenvalue decomposition [36–38],

$$\begin{bmatrix} 0 & \mathcal{B}\mathcal{B}^{\dagger} \\ \mathcal{C}^{\dagger}\mathcal{C} & 0 \end{bmatrix}\begin{bmatrix} \boldsymbol{\phi} \\ \boldsymbol{\psi} \end{bmatrix} \;=\; \gamma\begin{bmatrix} \mathcal{A} & 0 \\ 0 & \mathcal{A}^{\dagger} \end{bmatrix}\begin{bmatrix} \boldsymbol{\phi} \\ \boldsymbol{\psi} \end{bmatrix}, \tag{21}$$

where we suppress the dependence on $\{\boldsymbol{\kappa}, \omega, We, \beta, y\}$ for brevity. The eigenvalues $\gamma = \pm\sigma$ yield the singular values, and $\boldsymbol{\psi}$ is the vector of adjoint variables corresponding to $\boldsymbol{\phi}$ in (6).

The eigenvalue problem (21) consists of differential (infinite-dimensional) operators that act on continuous functions, $\boldsymbol{\phi}$ and $\boldsymbol{\psi}$. The operators in (21) are discretized using two well-conditioned spectral methods: the spectral integration method [36,39,40], and the ultraspherical method [41]. We now briefly discuss spectral methods and their well-conditioned variants.

Spectral methods express a variable in a differential equation in a basis of orthogonal polynomials like the Chebyshev polynomials, e.g.,

$$u(y) \;=\; \sum_{i=0}^{\infty}{}' \, u_i\,T_i(y), \tag{22}$$

where u_i are the unknown spectral coefficients to be solved for, $T_i(y)$ are the ith Chebyshev polynomials of the first kind, and $\sum'$ denotes a summation whose first term is halved (this convention is commonly used in a Chebyshev basis [40,42]).

Expressions for higher derivatives of the variable $u(y)$ are derived by using a Chebyshev differentiation operator [40]. The differentiation operator produces ill-conditioned matrix approximations to differential operators in (21) [42] that yield erroneous results for calculations of the resolvent norm (13) at moderate to large We [32,36] (also see Chapter 3 of [35]).

The recently developed well-conditioned ultraspherical [41] and spectral integration [39] methods avoid using the differentiation operator. For example, the spectral integration method avoids the differentiation operator by expressing the highest derivative in a differential equation with a Chebyshev basis, and expressing lower derivatives with an integration operator. The highest derivative of u in (5) is of second order, hence the second derivative of u is expressed as

$$\frac{\mathrm{d}^2 u}{\mathrm{d}y^2} \;=\; \sum_{i=0}^{N}{}' \, u_i^{(2)}\, T_i(y). \tag{23}$$

Expressions for lower derivatives of u in (23) are obtained using the recurrence relation for the integration of Chebyshev polynomials [40],

$$\frac{\mathrm{d}u}{\mathrm{d}y} \;=\; \sum_{i=0}^{N}{}' \, u_i^{(1)}\, T_i(y) \;+\; c_0, \tag{24}$$

where c_0 is a constant of integration and

$$u_i^{(1)} \;=\; \begin{cases} \frac{1}{2i}\left(u_{i-1}^{(2)} - u_{i+1}^{(2)}\right), & 0 < i < N, \\ \frac{1}{2}\, u_1^{(2)}, & i = 0, \\ \frac{1}{2N}\, u_{i-1}^{(2)}, & i = N. \end{cases} \tag{25}$$

The constants of integration can be computed using the boundary conditions in (5d).

Similarly, the ultraspherical method expresses a variable and its derivatives in a basis of ultraspherical polynomials [41],

$$\frac{\mathrm{d}^n u}{\mathrm{d}y^n} \;=\; \sum_{k=1}^{N} k\, u_k^{(n)} \frac{\mathrm{d}^{n-1} C_{k-1}^{(1)}(y)}{\mathrm{d}y^{n-1}}, \tag{26}$$

where $C_k^{(\alpha)}$ is the kth ultraspherical polynomial of the α kind. The derivatives of ultraspherical polynomials in (26) are related through the recurrence relation [41],

$$\frac{\mathrm{d}C_k^{(\alpha)}}{\mathrm{d}y} \;=\; \begin{cases} 2\,\alpha\, C_{k-1}^{(\alpha+1)}, & k \geq 1, \\ 0, & k = 0, \end{cases} \tag{27}$$

which forms a well-conditioned mapping between the variable and its derivatives, unlike the differentiation operator used in conventional spectral methods [41].

The spectral integration method is implemented in Matlab [36] (also see Chapter 3 of [35]) to derive finite-dimensional approximations to (21) in both the evolution and descriptor forms (see (6) and Appendix A). The ultraspherical discretization in Chebfun [41,43] is used to derive a finite-dimensional approximation in the evolution form (see Appendix A.1). As these well-conditioned methods are relatively new, we are currently not aware of how to use the ultraspherical method with the descriptor form. For all calculations reported in this paper, the corresponding velocity and stress from the SVD (see (14) and (17)) are resolved to machine precision by using up to 15,000 basis functions with these well-conditioned spectral methods.

These two approaches (evolution form with the ultraspherical method, descriptor and evolution forms with the spectral integration method; see (6) and Appendix A) produce the same singular values (a few representative validations are given in Appendix B), confirming the accuracy of our results. Furthermore, at large We for 2D3C Couette flow, our results agree with the We and We^2 scaling of the velocity $\boldsymbol{v}$ and stress τ_{xx} singular values (Appendix B) reported in Figures 3 and 4 of [15].

4. Localized and square-integrated amplification of the stress

In this section, we show that spanwise-constant stress fluctuations (2D model) can be more amplified than streamwise-constant stress fluctuations (2D3C model) when a localized measure of disturbance amplification (see (20)) is used. This is in contrast to what happens when a square-integrated measure of disturbance amplification (see (10)) is used [12,14–16]. We consider square-integrated amplification in Section 4.1, and localized amplification in Section 4.2. We fix the viscosity ratio to a representative value of $\beta = 0.5$, and the frequency to $\omega = 0$. In Section 5, we discuss the influence of ω in more detail. The streamwise and spanwise wavenumbers (k_x and k_z, respectively) are set to fixed values as the results are qualitatively similar for other values.

4.1. Square-integrated amplification

Fig. 2 shows the principal singular values as a function of We for the 2D3C model ($k_x = 0$, $k_z = 1$) with $\beta = 0.5$ and $\omega = 0$. Fig. 2a shows the velocity singular values obtained from the SVD of $\mathcal{T}_v$ (see (14)), and there is a linear growth with We when $We > \sim 20$. Recall that the singular value provides a square-integrated measure of the velocity or the stress amplification, as discussed in Section 2.3 (see (10), (16) and (19)).

Fig. 2b shows the stress singular values obtained from the SVD of $\mathcal{T}_{xx}$ (see (17)). We observe in Fig. 2b that the stress singular value grows quadratically with We. The We and We^2 scaling of the velocity and stress singular values in Figs. 2a and 2b, respectively, are in agreement with the scaling arguments of Jovanović and Kumar [15].

Fig. 3 shows the principal singular values as a function of We for the 2D model ($k_x = 1$, $k_z = 0$) with $\beta = 0.5$ and $\omega = 0$. Fig. 3a shows the velocity singular values computed from the SVD of $\mathcal{T}_v$ (see (14)). The singular value grows at relatively small We ($<\sim 5$) and then decays at larger We. As discussed in Section 2.3, the principal singular value gives the maximum possible kinetic energy of the velocity fluctuations for any square-integrable body force. We conclude from Fig. 3a that this maximum energy decreases with an increase in fluid elasticity for large enough We.

The stress singular values in Fig. 3b (the maximum possible square-integrated stress (10)) computed from the SVD of $\mathcal{T}_{xx}$ (see (17)) show a different trend. The singular value grows with an increase in We until $We \sim 20$, and then plateaus at large We.

As noted earlier, square-integrated measures are typically used in nonmodal analysis to characterize amplification of disturbances. From this perspective, the 2D3C model would exhibit a larger amplification than the 2D model at high We since the principal singular values of the 2D3C model grow with We whereas those of the 2D model do not. However, if a localized measure of disturbance amplification is employed, then the 2D model can show more amplification as we will demonstrate next.

4.2. Localized amplification

Fig. 4a shows $\hat{\tau}_{xx}$ (see (17) and (18)) corresponding to the principal singular value for the 2D3C model using the same parameters as in Fig. 2b with $We = 100$. Fig. 4b shows $\hat{\tau}_{xx}$ corresponding to the principal singular value for the 2D model using the same parameters as in Fig. 3b with $We = 100$. Fig. 4c enlarges the region near $y = 1$ in Fig. 4b for clarity.

The principal singular value for the 2D3C model ($\sigma_0 = 9422.386$; Fig. 4a) is about a thousand times greater than that for the 2D model ($\sigma_0 = 6.033$; Fig. 4b). However, the peak magnitude of the stress (see (18) and (20)) for the 2D3C model (Fig. 4a) is $\sigma_0\,|\hat{\tau}_{xx}|_{\max} \approx 9422.386 \times 0.01 \approx 94.22$. In contrast, for the 2D model (Figs. 4b and 4c) $\sigma_0\,|\hat{\tau}_{xx}|_{\max} \approx 6.033 \times 300 \approx 1810$; this is about twenty times larger than that of the 2D3C model.

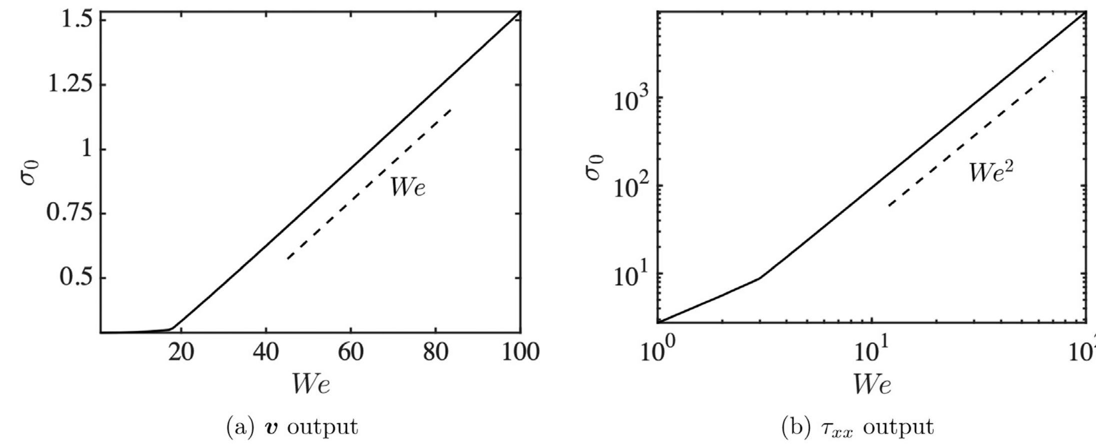

Fig. 2. Principal singular values of (a) $\mathcal{T}_v$ in (14) and (b) $\mathcal{T}_{xx}$ in (17) for the 2D3C model with $\beta = 0.5$, $k_z = 1$, and $\omega = 0$. The solid lines denote singular values, and the dashed lines show the scaling with We.

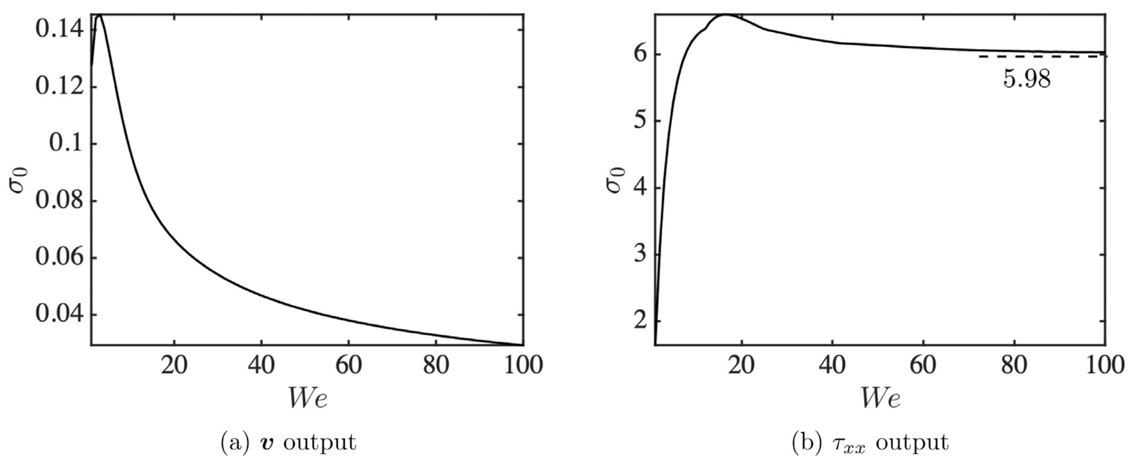

Fig. 3. Principal singular values of (a) $\mathcal{T}_v$ in (14) and (b) $\mathcal{T}_{xx}$ in (17) for the 2D model with $\beta = 0.5$, $k_x = 1$, and $\omega = 0$. The solid lines denote singular values, and the dashed line in (b) shows the magnitude of the singular value when $We = 500$.

In Fig. 4, both, the 2D3C and 2D models have body forces with unit $L^2[-1\ 1]$ norms (11), but the 2D model generates larger localized stress amplification compared to the 2D3C model under the same conditions. Therefore, we conclude from Fig. 4 that if we use a localized measure of disturbance amplification (see (20)) instead of a square-integrated measure (see (10)), the 2D model produces greater stress amplification compared to the 2D3C model. It should also be observed from Figs. 4b and 4c that the stress is highly localized near the channel boundaries. In addition, the velocity amplification is relatively weak as can be inferred from Fig. 3a.

Figs. 5a and 5b show the components of the velocity $\boldsymbol{v} = [u\ \ v]^T$ corresponding to the principal singular value of the 2D model. The magnitude of the velocity is $\mathcal{O}(0.1)$. This is about five orders of magnitude weaker than the maximum value of the stress, which as noted earlier is $\sigma_0\, |\hat{\tau}_{xx}|_{\max} \approx 6.033 \times 300 \approx 1810$ (Figs. 4b and 4c).

Our results thus demonstrate that polymer-stress fluctuations can be significantly amplified even if velocity fluctuations undergo negligible amplification. These amplified stresses and the corresponding gradients could put the system into a regime where nonlinear terms are no longer negligible, and this could lead to a flow transition. Such a mechanism might not be apparent from experimental observations, where velocity rather than stress fluctuations are typically measured. Because the stress fluctuations are highly localized, this alternative linear mechanism would be overlooked when using a square-integrated measure of disturbance amplification, which predicts that streamwise-constant fluctuations are most amplified. However, by using a localized measure of disturbance amplification, we find instead that spanwise-constant fluctuations are most amplified.

Figs. 5c and 5d show the x- and y-components of the body force that induce the velocities in Figs. 5a and 5b, and the stress in Figs. 4b and 4c. The magnitude of the x-component of the body force in Fig. 5c is significantly larger compared to the y-component in Fig. 5d. However, both components of the body force are localized near $y = \pm 1$, which are the same locations where the stress is localized (Figs. 4b and 4c). Since the maximum magnitude of the body force is $\mathcal{O}(100)$ and the maximum value of the stress fluctuation is $\mathcal{O}(1000)$, the stress fluctuation is amplified by an order of magnitude.

In Fig. 6 we plot in physical space contours of the kinetic energy $u^2 + v^2$; and the square of the stress τ_{xx}^2 that result from the body force shown in Figs. 5c and 5d. Recall that the persistent body force we use (see (5e)) is localized in x and z. Plots in physical space are obtained by applying an inverse Fourier transform to the velocity and stress by linearly sampling 24 wavenumbers from $k_{x,\min} = -2.5$ to $k_{x,\max} = 2.29$, and using 6000 Chebyshev basis functions in the y-direction. Red represents regions of high magnitude, and blue represents regions of low magnitude as indicated in the color bars.

We observe in Fig. 6a that the kinetic energy, u^2+v^2; has a peak value near the channel center at $y = 0$ of $\mathcal{O}(10^{-3})$. This is consistent with the observations in Figs. 5a and 5b where the magnitude of the velocity in Fourier space is the largest near the channel center ($y = 0$) and smaller near the channel walls ($y = \pm 1$). Figs. 6b, 6c and 6d consider the square of the stress, τ_{xx}^2. Fig. 6b is almost entirely blue, which corresponds to

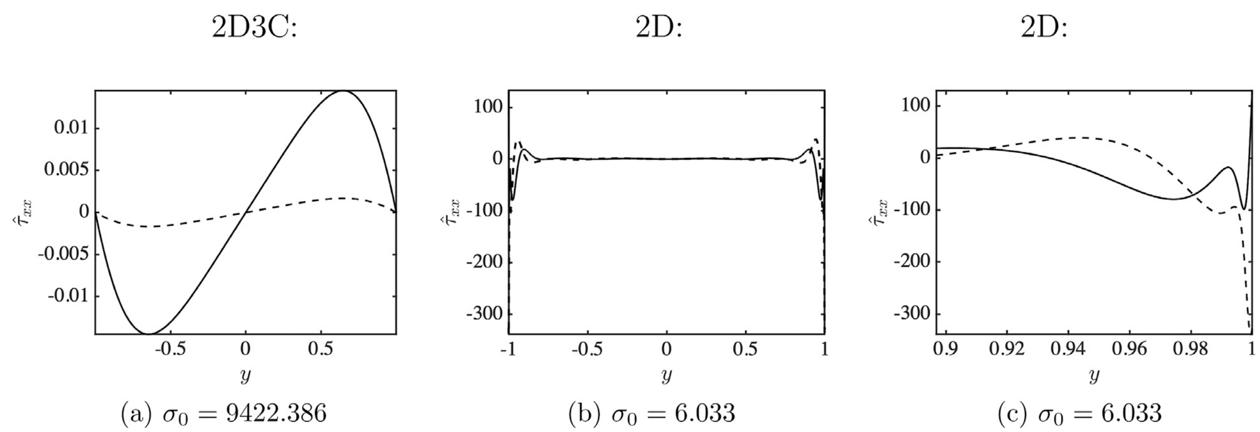

Fig. 4. The quantity $\hat{\tau}_{xx}$ (see (18)) corresponding to the principal singular value from the SVD of $\mathcal{T}_{xx}$ in (17) for the (a) 2D3C ($k_z = 1$), and (b,c) 2D ($k_x = 1$) models with $We = 100$, $\beta = 0.5$, and $\omega = 0$. Solid lines denote the real parts and dashed lines denote the imaginary parts of $\hat{\tau}_{xx}$. Panel (c) enlarges panel (b) near $y = 1$.

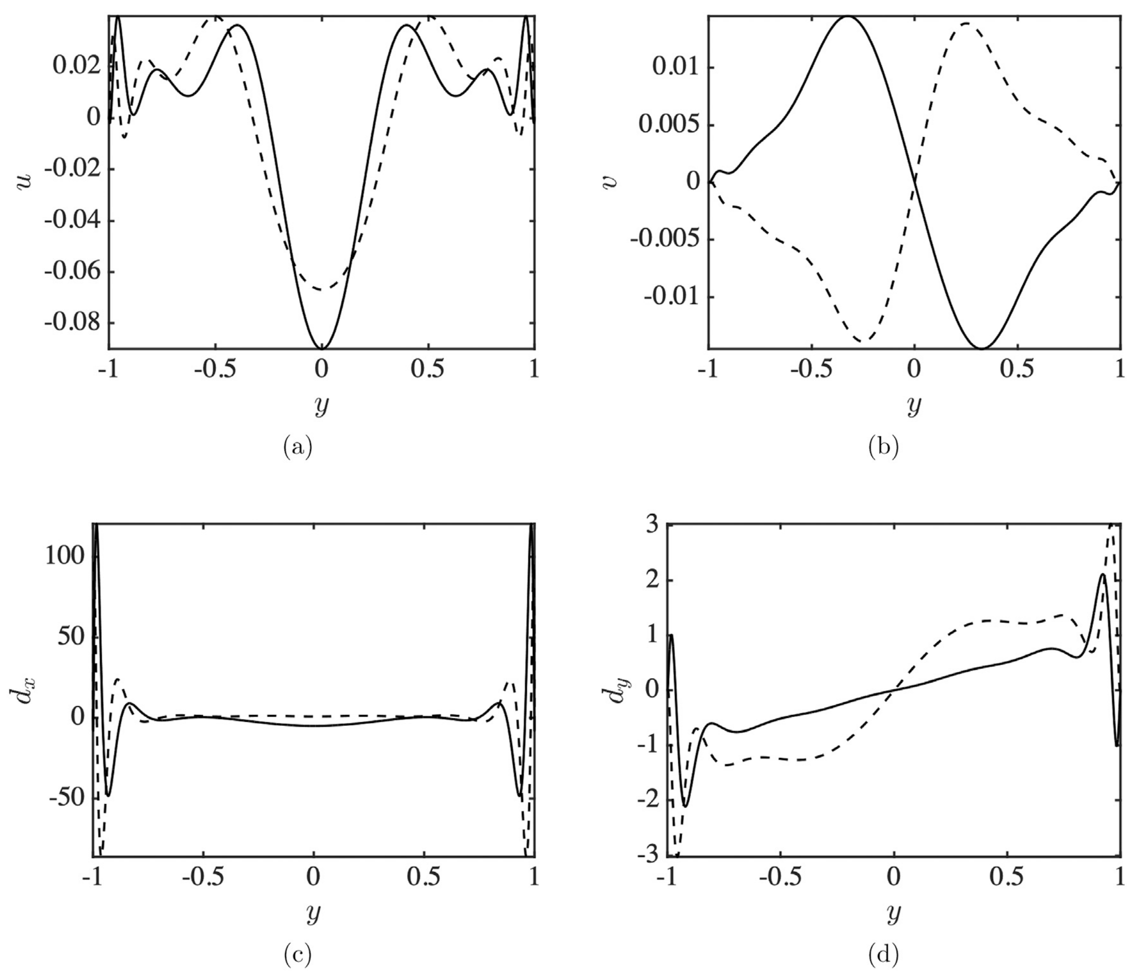

Fig. 5. The (a,b) velocity components $\boldsymbol{v} = [u \;\; v]^T$, and (c,d) x- and y-components of the body force $\boldsymbol{d}$, corresponding to the principal singular value from the SVD of $\mathcal{T}_{xx}$ in (17) of 2D model with $We = 100$, $\beta = 0.5$, $k_x = 1$, and $\omega = 0$. Solid lines denote the real parts and dashed lines denote the imaginary parts of the velocity and body force.

near-zero values. This is because the stress is highly localized near the walls ($y = \pm 1$). This can be observed in Figs. 6c and 6d, where Fig. 6b is enlarged in the regions near $y = -1$ and $y = +1$ respectively. Both $u^2 + v^2$ and τ_{xx}^2 are also localized around $x = 0$, with a weak presence upstream and downstream.

The color bars in Figs. 6b, 6c and 6d indicate that the square of the stress reaches a value of $\mathcal{O}(10^6)$. This large value is prominent near the channel walls at $y = \pm 1$, as seen in Figs. 6c and 6d. Furthermore, the kinetic energy ($\mathcal{O}(10^{-3})$ in Fig. 6a) and the square of the stress ($\mathcal{O}(10^6)$ in Figs. 6b, 6c and 6d) have a disparity of about nine orders of magnitude, again highlighting that stress fluctuations can undergo considerably more amplification even when there is negligible amplification of velocity fluctuations.

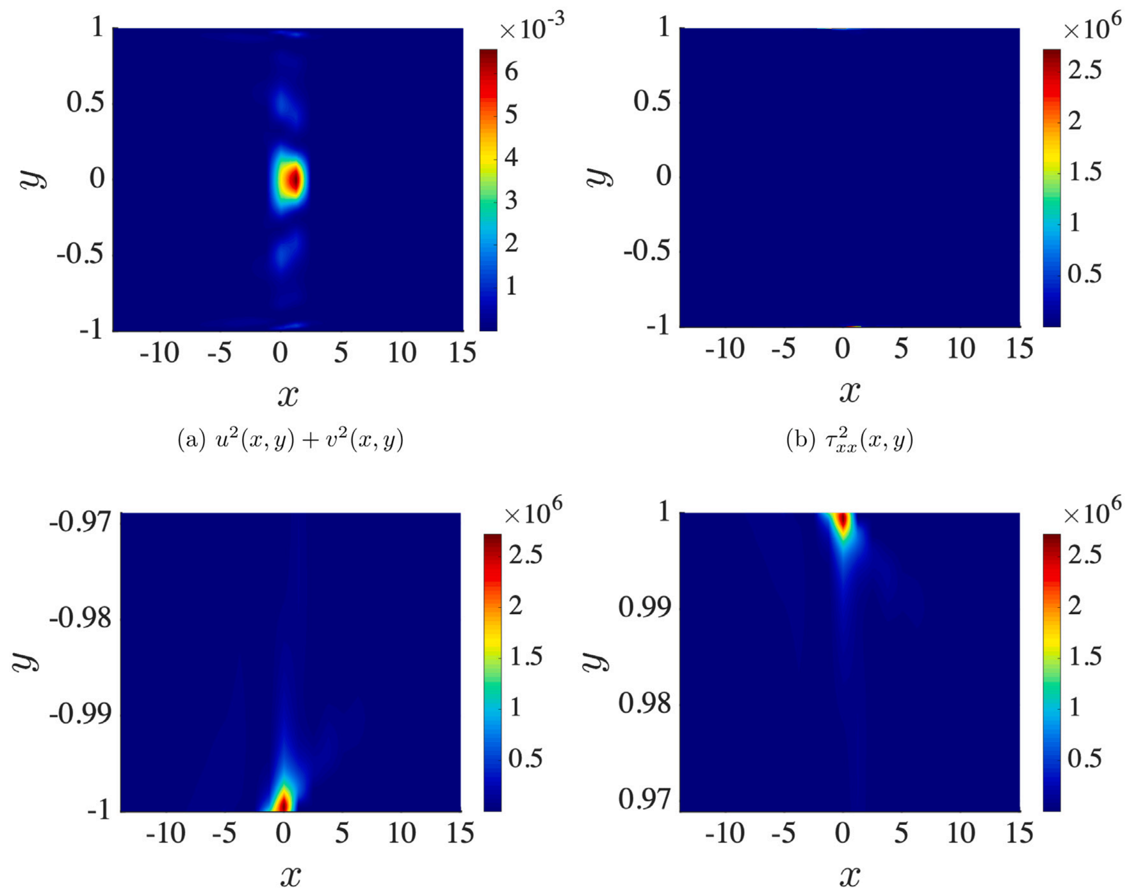

(a) $u^2(x,y)+v^2(x,y)$ (b) $\tau_{xx}^2(x,y)$

(c) $\tau_{xx}^2(x,y)$ (d) $\tau_{xx}^2(x,y)$

Fig. 6. The steady-state (a) kinetic energy u^2+v^2 and (b,c,d) squared stress τ_{xx}^2 that result from a persistent body force in the 2D model of the form in (5e) with a frequency $\omega = 0$ and a variation in y shown in Figs. 5c and 5d. Here, $We = 100$ and $\beta = 0.5$. Panel (c) enlarges panel (b) near $y = -1$, and panel (d) enlarges panel (b) near $y = 1$. (For interpretation of the references to color in this figure legend, the reader is referred to the web version of this article.)

5. Role of continuous spectrum in stress amplification

In this section we demonstrate that localized amplification of the stress (Figs. 4b and 4c) arises from the continuous spectrum $\lambda(y) = -i\,k_x\,\bar{U}(y) - 1/We$ (see (7c)) of the linearized problem. Note that the continuous spectrum reverts to a discrete eigenvalue $\lambda = -1/We$ by setting $k_x = 0$. It should be noted that although the continuous spectrum arises from a modal analysis, which is not what is being done in the present work, we retain the term here for simplicity since $\lambda(y)$ appears in our nonmodal analysis.

The expression for τ_{xx} for the full 3D system (see (6c) and (A.3)) is given by

$$\tau_{xx} = c_{1,11}\mathrm{D}u + c_{0,11}u + c_{1,12}\mathrm{D}v + c_{0,12}v, \tag{28}$$

where $\mathrm{D} := \mathrm{d}/\mathrm{d}y$. Note that this expression also holds for the 2D model since (28) is k_z- and w-independent, where w is the z-component of $\boldsymbol{v}$. The expression for τ_{xx} for the 2D3C model can be derived by setting $k_x = 0$ in (28).

To illustrate key points, we focus on the first term, $c_{1,11}$ in (28),

$$c_{1,11}\mathrm{D}u = \frac{2\left(We\,c(y)\bar{T}_{xy}(y) + \bar{U}'(y)\right)}{We\,c(y)^2}\mathrm{D}u. \tag{29}$$

where

$$c(y) = i\,\omega + 1/We + i\,k_x\,\bar{U}(y). \tag{30}$$

Note that $c(y) = i\omega - \lambda(y)$ where $\lambda(y)$ is the continuous spectrum (see (7c)).

Eq. (29) can be rearranged as

$$c_{1,11}\mathrm{D}u = \underbrace{\frac{2\,\bar{T}_{xy}(y)}{i\,\omega + \frac{1}{We} + i\,k_x\,\bar{U}(y)}}_{g_1(y,\omega,k_x,We)}\mathrm{D}u + \underbrace{\frac{2\,\bar{U}'(y)}{We(i\,\omega + \frac{1}{We} + i\,k_x\,\bar{U}(y))^2}}_{g_2(y,\omega,k_x,We)}\mathrm{D}u. \tag{31}$$

In (31), $\bar{T}_{xy}$ and $\bar{U}'(y)$ are the same, i.e., $\bar{T}_{xy} = \bar{U}'(y)$ (see (4)), but we retain them separately to identify which couplings between base-state and fluctuation quantities give rise to them. The contribution from $\bar{T}_{xy}$ in (31) comes from $\bar{\boldsymbol{T}}\cdot\nabla\boldsymbol{v}$ in (5c), and that from $\bar{U}'(y)$ in (31) comes from $\boldsymbol{\tau}\cdot\nabla\bar{\boldsymbol{V}}$ in (5c). In what follows, we will focus on g_1 since g_2 exhibits similar behavior. Indeed, all the functions $c_{1,11}$, $c_{0,11}$, $c_{1,12}$, and $c_{0,12}$ in (28) contain $c(y)$ or its powers in the denominator (see (A.4)) and thus exhibit behavior similar to g_1 in (31).

We next plot g_1 in (31) to understand its role in generating localized amplification in τ_{xx} (Figs. 4b and 4c). Fig. 7 shows g_1 under the same conditions as Fig. 4, i.e., with $We = 100$, $k_x = 1$, and $\omega = 0$. Note that g_1 in (31) is k_z- and β-independent.

For the 2D model, we observe from Figs. 7a and 7b that g_1 shows localized amplification near $y = \pm 1$. Fig. 7b enlarges Fig. 7a near $y = 1$ for clarity, and we observe that g_1 has a maximum magnitude of ~ 400. Furthermore, the locations of localized amplification of $\hat{\tau}_{xx}$ in Figs. 4b and 4c are near $y = \pm 1$, and this is where g_1 is also locally amplified in Figs. 7a and 7b.

In Fig. 7c we plot g_1 for the 2D3C model ($k_z = 1$, in which case $g_1(y) = -2\,We\,\bar{U}'(y)$), and we observe a smooth function without prominent localized amplification. This is again similar to the 2D3C

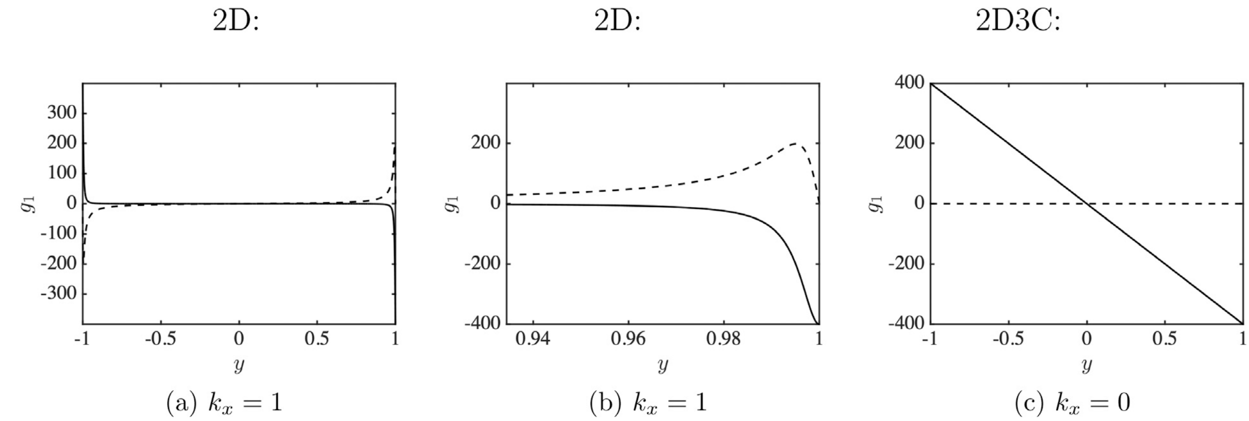

Fig. 7. The function g_1 in (31) with $We = 100$, and $\omega = 0$ (a,b) $k_x = 1$, and (c) $k_z = 1$. The solid lines mark the real parts and the dashed lines mark the imaginary parts of g_1. Panel (b) enlarges panel (a) near $y = 1$.

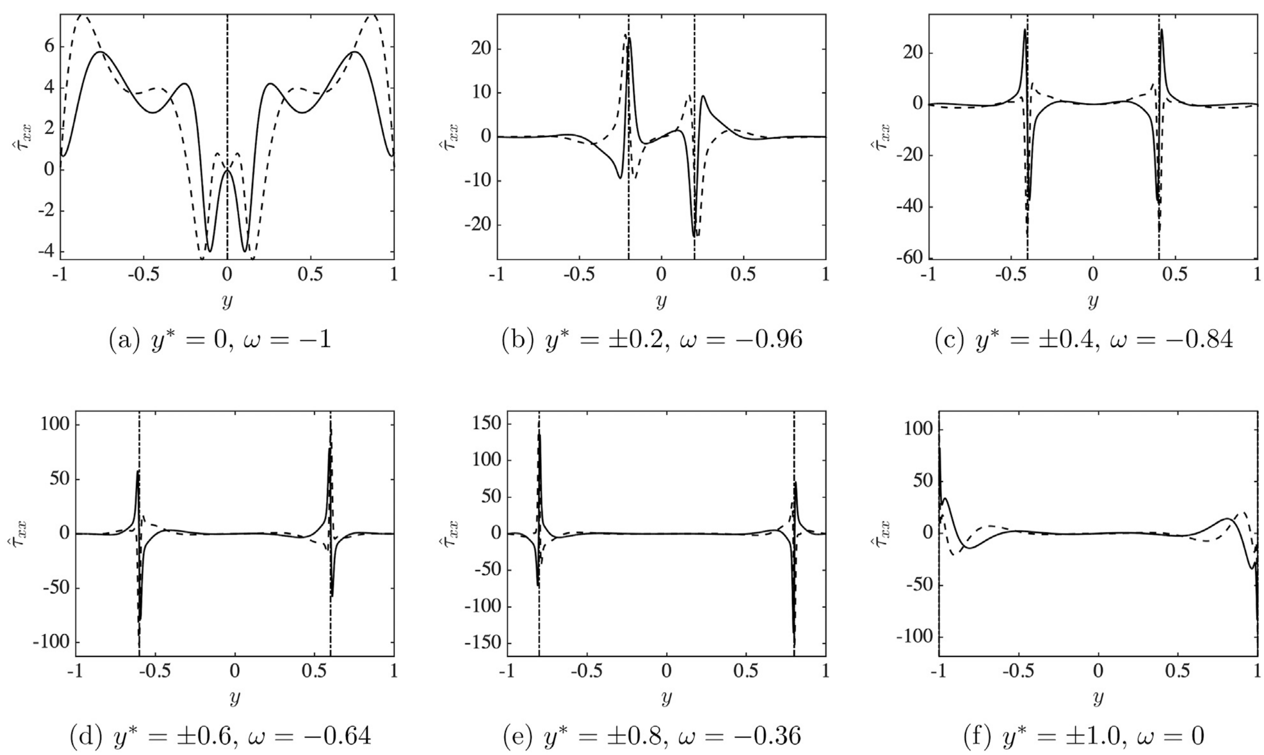

Fig. 8. The quantity τ_{xx} corresponding to the principal singular value from the SVD of $\mathcal{T}_{xx}$ in (17) with $We = 40$, $\beta = 0.5$, and $k_x = 1$, and (a) $y^* = 0$, (b) $y^* = \pm 0.2$, (c) $y^* = \pm 0.4$, (d) $y^* = \pm 0.6$, (e) $y^* = \pm 0.8$, and (f) $y^* = \pm 1$. For given values of k_x and y^*, ω is calculated from (33). The solid lines mark the real parts and the dashed lines mark the imaginary parts of $\hat{\tau}_{xx}$. The dashed–dotted lines mark $y = y^*$.

case in Fig. 4a, where τ_{xx} is a smooth function without prominent localized amplification.

To gain further insight into the origin of the localized amplification of g_1 (Figs. 7a and 7b), we separate the real and imaginary parts of g_1 in (31), yielding

$$g_1(y) = \frac{2\,\bar{T}_{xy}(y)(1/We - i\,(\omega + k_x \bar{U}(y)))}{1/We^2 + (\omega + k_x \bar{U}(y))^2}. \tag{32}$$

For a finite numerator, the function g_1 in (32) reaches its largest magnitude when its denominator is at its minimum. As the denominator is a sum of two squares in (32), it is minimized when $y = y^*$ such that

$$\omega + k_x \bar{U}(y^*) = 0. \tag{33}$$

The location $y = y^*$ would then correspond to the place where we expect the magnitude of g_1 in (32), and thus the stress amplification, to be maximized. Note that $\omega + k_x \bar{U}(y)$ is the imaginary part of $c(y)$ (see (30)), and recall that $c(y) = i\omega - \lambda(y)$ where $\lambda(y)$ is the continuous spectrum (see (7c)).

Eq. (33) can be used to identify where localized amplification occurs (y^*) for given values of ω and k_x. For example, for the case shown in Fig. 7, substituting $\omega = 0$ and $k_x = 1$ in (33) yields $y^* = \pm 1$ since the base-state streamwise velocity $\bar{U}$ vanishes at the channel walls. As seen in Figs. 7a and 7b, g_1 is locally amplified near $y^* = \pm 1$, and as seen in Figs. 4b and 4c, the stress is locally amplified there as well. Note that for the 2D3C model, $k_x = 0$, and as a consequence, there are no longer specific points y^* where (33) is satisfied. This is consistent with the relatively weak localized amplification observed in Figs. 7c and 4a.

We now consider what happens for different values of ω. To do this we pick several values of $y^* \in [-1,\ 1]$ in the channel, fix $k_x = 1$ (with $We = 40$ and $\beta = 0.5$), and calculate ω from (33). We then use this value of ω and compute a SVD of $\mathcal{T}_{xx}$ in (17). In Fig. 8, the solid and dashed lines mark the real and imaginary parts of $\hat{\tau}_{xx}$ (see (17)) corresponding to the principal singular value from the SVD of $\mathcal{T}_{xx}$, and the dashed-dotted lines mark $y = y^*$. If the dashed-dotted lines match the locations where localized amplification occurs for $\hat{\tau}_{xx}$, this would further support the idea that (33), which is related to the continuous spectrum, can be used to identify where localized stress amplification occurs.

Figs. 8b–8f show excellent agreement between the predictions of (33) and the numerical results for values of y^* away from the channel centerline, thus demonstrating the key role that the continuous spectrum plays in localized stress amplification. We note that the case where $y^* = 0$ shown in Fig. 8a is an exception. This can be understood by recognizing that the numerator of g_1 in (31) vanishes when $y = y^* = 0$ since $\bar{T}_{xy} = \bar{U}'(y) = -2y$. Further discussion of this case can be found in [35]. We also see from Fig. 8 that as the frequency increases in magnitude, the location of the amplification moves toward the channel center. In addition, the amplitude of the magnification is generally larger for smaller frequency magnitudes.

Although we have presented results for $k_x = 1$, similar behavior has been observed at other values of k_x as well [35]. The localized stress amplification we have uncovered arises from coupling between base-state and fluctuation quantities, as was pointed out when describing (31). However, computational limitations have prevented us from fully exploring the (k_x, ω, We) parameter space, so we cannot draw more detailed conclusions at this time regarding which couplings are most prominent in various regions of the parameter space. Note that the stress functions from the SVD (see (18)) become increasingly steep with an increase in k_x (> 3) and need a large number of basis functions for good resolution, making SVD (17) prohibitively expensive. Nevertheless, it is clear from the above discussion that the continuous spectrum plays a key role in generating localized stress amplification.

Finally, we note that as $We \to \infty$, the minimum value of the denominator of (32) is 0, in which case $|\tau_{xx}|_{\max} \to \infty$ at specific points $y = y^*$ in the channel (from (33)). This arises from the infinite extensibility of the Hookean dumbbells used to represent polymer molecules in the Oldroyd-B constitutive equation. Although the singular values for the 2D model were observed to plateau with large We in Fig. 3b, the peak magnitude of the function $|\hat{\tau}_{xx}|_{\max} \to \infty$ as $We \to \infty$. In contrast, localized amplification is not as prominent for the 2D3C model, as discussed above. However, the singular values themselves tend to infinity as $We \to \infty$ as seen in Fig. 2b. Accounting for the finite extensibility of the polymer molecules (e.g., by using the FENE-CR constitutive equation) may put bounds on the level of disturbance amplification but is not expected to lead to qualitative changes in the results observed here based on prior nonmodal analysis of viscoelastic channel flows [16].

6. Conclusions

Our results demonstrate that in channel flows of viscoelastic fluids subject to a localized time-periodic body force, spanwise-constant polymer-stress fluctuations can undergo enormous amplification. This amplification is highly localized in space, and was overlooked in prior studies that used square-integrated measures of disturbance amplification, which are typically applied in nonmodal analysis. By using a localized measure of disturbance amplification, we find that spanwise-constant stress fluctuations are more amplified than streamwise-constant stress fluctuations. This amplification appears to arise from the continuous spectrum of the linearized problem, with the amplification location depending on the frequency of the body force.

Our findings may be useful for understanding the experimental observations of Pan et al. and Qin et al. [3,4] involving microchannel flows of viscoelastic fluids. In those experiments, the cylinders that perturb the flow create a localized, time-periodic disturbance, and the magnitude of velocity fluctuations decreases downstream before increasing. Although there is significant stress amplification in our model problem, we find that there is negligible amplification of velocity fluctuations, which seems consistent with the experiments. The large stress amplification we observe could put the flow into a regime where nonlinear terms are no longer negligible, and this could trigger a transition to elastic turbulence.

The large localized stress amplification we observe is unexpected, unique to viscoelastic fluids, and represents an alternate linear mechanism by which finite-amplitude perturbations can be generated. Our results also provide fundamental information about the frequency response of inertialess viscoelastic channel flows. Definitively unraveling the full mechanisms through which elastic turbulence is generated in such flows will require nonlinear simulations, an outstanding challenge in non-Newtonian fluid mechanics. The well-conditioned spectral methods we apply here may be especially well-suited for this task because of their ability to resolve sharp stress gradients.

Declaration of competing interest

The authors declare that they have no known competing financial interests or personal relationships that could have appeared to influence the work reported in this paper.

Acknowledgments

This work is supported in part by the National Science Foundation, United States under grant number CBET-1510654. The Minnesota Supercomputing Institute (MSI) at the University of Minnesota is acknowledged for providing computing resources.

Appendix A. Operators governing channel flow of an Oldroyd-B fluid

The equations governing channel flow of an Oldroyd-B fluid (5) can be recast to the representation in (6) as discussed in Section 2.1. System (6) can be expressed in two forms, the evolution form (where the pressure is eliminated), and the descriptor form (where the pressure is not eliminated). In this section we present the operators $\mathcal{A}$, $\mathcal{B}$, $\mathcal{C}_v$, and $\mathcal{C}_{xx}$ in (6) in both forms.

A.1. Evolution form

The state variables for the evolution form [21] are the wall-normal velocity and vorticity, $\boldsymbol{\phi} = [\, v \;\, \eta \,]^T$ in (6). The boundary conditions are

$$v(\pm 1) \;=\; [\mathrm{D}v(\cdot)](\pm 1) \;=\; \eta(\pm 1) \;=\; 0. \tag{A.1}$$

The operator-valued matrices $\mathcal{A}$, $\mathcal{B}$, $\mathcal{C}_v$, and $\mathcal{C}_{xx}$ are detailed in this section. $\mathcal{A}$ is of size 2×2 with elements

$$\begin{aligned}
\mathcal{A}(1,1) &= \left(\sum_{n=0}^{4} a_{n,11}(y,\omega) \mathrm{D}^n \right), \\
\mathcal{A}(1,2) &= 0, \\
\mathcal{A}(2,1) &= \left(\sum_{n=0}^{2} a_{n,21}(y,\omega) \mathrm{D}^n \right), \\
\mathcal{A}(2,2) &= \left(\sum_{n=0}^{2} a_{n,22}(y,\omega) \mathrm{D}^n \right),
\end{aligned}$$

where the dependence on ω enters through the $c(y)$ in (30), and the nonzero coefficients $a_{n,ij}$ are given by

$$\begin{aligned}
a_{4,11} &= -\frac{(1-\beta)}{We\, c(y)} - \beta, \\
a_{3,11} &= \frac{2(1-\beta)\, c'(y)}{We\, c(y)^2} - \frac{2i(1-\beta)\, k_x\, \bar{T}_{xy}(y)}{c(y)},
\end{aligned}$$

$$
\begin{aligned}
a_{2,11} \;=\;& \frac{(1-\beta)\,c''(y)}{We\,c(y)^2} + \frac{2i(1-\beta)\,k_x\,\bar{T}_{xy}(y)c'(y)}{c(y)^2} - \frac{4i(1-\beta)\,k_x\,c'(y)\bar{U}'(y)}{We\,c(y)^3} \\
&- \frac{2(1-\beta)\,c'(y)^2}{We\,c(y)^3} + \frac{2(1-\beta)\,k^2}{We\,c(y)} + \frac{(1-\beta)\,k_x^2\,\bar{T}_{xx}(y)}{c(y)} \\
&- \frac{2(1-\beta)\,k_x^2\,\bar{T}_{xy}(y)\bar{U}'(y)}{c(y)^2} - \frac{4(1-\beta)\,k_x^2\,\bar{U}'(y)^2}{We\,c(y)^3} \\
&- \frac{3i(1-\beta)\,k_x\,\bar{T}'_{xy}(y)}{c(y)} + \frac{2i(1-\beta)\,k_x\,\bar{U}''(y)}{We\,c(y)^2} + 2\beta\,k^2, \\
a_{1,11} \;=\;& -\frac{4i(1-\beta)\,k_x\,c''(y)\bar{U}'(y)}{We\,c(y)^3} + \frac{8(1-\beta)\,k_x^2\,\bar{T}_{xy}(y)c'(y)\bar{U}'(y)}{c(y)^3} \\
&+ \frac{12(1-\beta)\,k_x^2\,c'(y)\bar{U}'(y)^2}{We\,c(y)^4} - \frac{2(1-\beta)\,k_x^2\,c'(y)}{We\,c(y)^2} \\
&+ \frac{2i(1-\beta)\,k_x\,c'(y)\bar{T}'_{xy}(y)}{c(y)^2} \\
&- \frac{8i(1-\beta)\,k_x\,c'(y)\bar{U}''(y)}{We\,c(y)^3} + \frac{12i(1-\beta)\,k_x\,c'(y)^2\bar{U}'(y)}{We\,c(y)^4} \\
&- \frac{2(1-\beta)\,k_z^2\,c'(y)}{We\,c(y)^2} \\
&+ \frac{2i(1-\beta)\,k^2\,k_x\,\bar{T}_{xy}(y)}{c(y)} - \frac{2i(1-\beta)\,k_x^3\,\bar{T}_{xx}(y)\bar{U}'(y)}{c(y)^2} \\
&- \frac{4i(1-\beta)\,k_x^3\,\bar{T}_{xy}(y)\bar{U}'(y)^2}{c(y)^3} + \frac{(1-\beta)\,k_x^2\,\bar{T}'_{xx}(y)}{c(y)} \\
&- \frac{2(1-\beta)\,k_x^2\,\bar{T}'_{xy}(y)\bar{U}'(y)}{c(y)^2} - \frac{4(1-\beta)\,k_x^2\,\bar{T}_{xy}(y)\bar{U}''(y)}{c(y)^2} \\
&- \frac{8(1-\beta)\,k_x^2\,\bar{U}'(y)\bar{U}''(y)}{We\,c(y)^3},
\end{aligned}
$$

$$
\begin{aligned}
a_{0,11} \;=\;& \frac{(1-\beta)\,k^2\,c''(y)}{We\,c(y)^2} + \frac{(1-\beta)\,k_x^2\,\bar{T}_{xx}(y)c''(y)}{c(y)^2} \\
&+ \frac{4(1-\beta)\,k_x^2\,\bar{T}_{xy}(y)c''(y)\bar{U}'(y)}{c(y)^3} \\
&+ \frac{i(1-\beta)\,k_x\,c''(y)\bar{T}'_{xy}(y)}{c(y)^2} - \frac{2i(1-\beta)\,k^2\,k_x\,\bar{T}_{xy}(y)c'(y)}{c(y)^2} \\
&+ \frac{4i(1-\beta)\,k^2\,k_x\,c'(y)\bar{U}'(y)}{We\,c(y)^3} - \frac{2(1-\beta)\,k^2\,c'(y)^2}{We\,c(y)^3} \\
&+ \frac{4i(1-\beta)\,k_x^3\,\bar{T}_{xx}(y)c'(y)\bar{U}'(y)}{c(y)^3} \\
&+ \frac{12i(1-\beta)\,k_x^3\,\bar{T}_{xy}(y)c'(y)\bar{U}'(y)^2}{c(y)^4} + \frac{(1-\beta)\,k_x^2\,c'(y)\bar{T}'_{xx}(y)}{c(y)^2} \\
&- \frac{2(1-\beta)\,k_x^2\,\bar{T}_{xx}(y)c'(y)^2}{c(y)^3} + \frac{4(1-\beta)\,k_x^2\,c'(y)\bar{T}'_{xy}(y)\bar{U}'(y)}{c(y)^3} \\
&+ \frac{8(1-\beta)\,k_x^2\,\bar{T}_{xy}(y)c'(y)\bar{U}''(y)}{c(y)^3} - \frac{12(1-\beta)\,k_x^2\,\bar{T}_{xy}(y)c'(y)^2\bar{U}'(y)}{c(y)^4} \\
&- \frac{2i(1-\beta)\,k_x\,c'(y)^2\bar{T}'_{xy}(y)}{c(y)^3} - \frac{(1-\beta)\,k^4}{We\,c(y)} - \frac{(1-\beta)\,k^2\,k_x^2\,\bar{T}_{xx}(y)}{c(y)} \\
&- \frac{2(1-\beta)\,k^2\,k_x^2\,\bar{T}_{xy}(y)\bar{U}'(y)}{c(y)^2} + \frac{i(1-\beta)\,k^2\,k_x\,\bar{T}'_{xy}(y)}{c(y)} \\
&- \frac{2i(1-\beta)\,k^2\,k_x\,\bar{U}''(y)}{We\,c(y)^2} \\
&- \frac{2i(1-\beta)\,k_x^3\,\bar{T}'_{xx}(y)\bar{U}'(y)}{c(y)^2} - \frac{2i(1-\beta)\,k_x^3\,\bar{T}_{xx}(y)\bar{U}''(y)}{c(y)^2} \\
&- \frac{4i(1-\beta)\,k_x^3\,\bar{T}'_{xy}(y)\bar{U}'(y)^2}{c(y)^3} - \frac{8i(1-\beta)\,k_x^3\,\bar{T}_{xy}(y)\bar{U}'(y)\bar{U}''(y)}{c(y)^3} \\
&- \frac{2(1-\beta)\,k_x^2\,\bar{T}'_{xy}(y)\bar{U}''(y)}{c(y)^2} - \beta k^4, \\
a_{2,21} \;=\;& -\frac{i(1-\beta)\,k_z\,\bar{U}'(y)}{We\,c(y)^2},
\end{aligned}
$$

$$
\begin{aligned}
a_{1,21} \;=\;& \frac{i(1-\beta)\,k_z\,\bar{T}_{xy}(y)c'(y)}{c(y)^2} + \frac{4i(1-\beta)\,k_z\,c'(y)\bar{U}'(y)}{We\,c(y)^3} \\
&+ \frac{3(1-\beta)\,k_x\,k_z\,\bar{T}_{xy}(y)\bar{U}'(y)}{c(y)^2} \\
&+ \frac{4(1-\beta)\,k_x\,k_z\,\bar{U}'(y)^2}{We\,c(y)^3} - \frac{2i(1-\beta)\,k_z\,\bar{U}''(y)}{We\,c(y)^2}, \\
a_{0,21} \;=\;& -\frac{(1-\beta)\,k_x\,k_z\,\bar{T}_{xx}(y)c'(y)}{c(y)^2} - \frac{4(1-\beta)\,k_x\,k_z\,\bar{T}_{xy}(y)c'(y)\bar{U}'(y)}{c(y)^3} \\
&- \frac{i(1-\beta)\,k_z\,c'(y)\bar{T}'_{xy}(y)}{c(y)^2} + \frac{2i(1-\beta)\,k_x^2\,k_z\,\bar{T}_{xx}(y)\bar{U}'(y)}{c(y)^2} \\
&+ \frac{4i(1-\beta)\,k_x^2\,k_z\,\bar{T}_{xy}(y)\bar{U}'(y)^2}{c(y)^3} + \frac{i(1-\beta)\,k_x^2\,k_z\,\bar{U}'(y)}{We\,c(y)^2} \\
&+ \frac{2(1-\beta)\,k_x\,k_z\,\bar{T}_{xy}(y)\bar{U}''(y)}{c(y)^2} + \frac{i(1-\beta)\,k_z^3\,\bar{U}'(y)}{We\,c(y)^2},
\end{aligned}
$$

$$
\begin{aligned}
a_{2,22} \;=\;& -\frac{(1-\beta)}{We\,c(y)} - \beta, \\
a_{1,22} \;=\;& \frac{(1-\beta)\,c'(y)}{We\,c(y)^2} - \frac{2i(1-\beta)\,k_x\,\bar{T}_{xy}(y)}{c(y)} - \frac{i(1-\beta)\,k_x\,\bar{U}'(y)}{We\,c(y)^2}, \\
a_{0,22} \;=\;& \frac{i(1-\beta)\,k_x\,\bar{T}_{xy}(y)c'(y)}{c(y)^2} + \frac{(1-\beta)\,k^2}{We\,c(y)} \\
&+ \frac{(1-\beta)\,k_x^2\,\bar{T}_{xx}(y)}{c(y)} + \frac{(1-\beta)\,k_x^2\,\bar{T}_{xy}(y)\bar{U}'(y)}{c(y)^2} \\
&- \frac{i(1-\beta)\,k_x\,\bar{T}'_{xy}(y)}{c(y)} + \beta k^2,
\end{aligned}
$$

where $c(y) = i\,\omega + 1/We + i\,k_x\,\bar{U}(y)$ (see (30)).

The operators $\mathcal{C}_v$ (for the velocity output) and $\mathcal{B}$ are given by [19]

$$
\mathcal{C}_v = \frac{1}{k^2}\begin{bmatrix} i\,k_x\,\mathrm{D} & -i\,k_z \\ k^2 & 0 \\ i\,k_z\,\mathrm{D} & i\,k_x \end{bmatrix}, \quad \mathcal{B} = \begin{bmatrix} -i\,k_x\,\mathrm{D} & -k^2 & -i\,k_z\,\mathrm{D} \\ i\,k_z & 0 & -i\,k_x \end{bmatrix}. \tag{A.2a}
$$

For the stress output τ_{xx}, $\mathcal{C}_{xx}$ is a 1×2 block-matrix operator with

$$
\begin{aligned}
\mathcal{C}_{xx}(1,1) \;=\;& \left(\sum_{n=0}^{2} c_{n,11}(y,\omega)\mathrm{D}^n\right), \\
\mathcal{C}_{xx}(1,2) \;=\;& \left(\sum_{n=0}^{1} c_{n,12}(y,\omega)\mathrm{D}^n\right),
\end{aligned} \tag{A.2b}
$$

where the nonzero coefficients $c_{n,ij}$ are given by

$$
\begin{aligned}
c_{2,11} \;=\;& \frac{2ik_x\,\bar{T}_{xy}(y)}{k^2\,c(y)} + \frac{2ik_x\,\bar{U}'(y)}{k^2\,We\,c(y)^2}, \\
c_{1,11} \;=\;& -\frac{2k_x^2\,\bar{T}_{xx}(y)}{k^2\,c(y)} - \frac{2k_x^2}{k^2\,We\,c(y)} + \frac{2k_z^2\,\bar{T}_{xy}(y)\bar{U}'(y)}{k^2\,c(y)^2} + \frac{4\bar{U}'(y)^2}{We\,c(y)^3}, \\
c_{0,11} \;=\;& \frac{2ik_x\,\bar{T}_{xx}(y)\bar{U}'(y)}{c(y)^2} + \frac{4ik_x\,\bar{T}_{xy}(y)\bar{U}'(y)^2}{c(y)^3} + \frac{2ik_x\,\bar{U}'(y)}{We\,c(y)^2} - \frac{\bar{T}'_{xx}(y)}{c(y)} \\
&- \frac{2\bar{T}'_{xy}(y)\bar{U}'(y)}{c(y)^2}, \\
c_{1,12} \;=\;& -\frac{2ik_z\,\bar{T}_{xy}(y)}{k^2\,c(y)} - \frac{2ik_z\,\bar{U}'(y)}{k^2\,We\,c(y)^2}, \\
c_{0,12} \;=\;& \frac{2k_x\,k_z\,\bar{T}_{xx}(y)}{k^2\,c(y)} + \frac{2k_x\,k_z\,\bar{T}_{xy}(y)\bar{U}'(y)}{k^2\,c(y)^2} + \frac{2k_x\,k_z}{k^2\,We\,c(y)}.
\end{aligned}
$$

A.2. Descriptor form

The state variables of the descriptor form are the velocity and pressure, i.e., $\boldsymbol{\phi} = [\,u\;v\;w\;p\,]^T$ in (6). The boundary conditions are

$$
u(\pm 1) \;=\; v(\pm 1) \;=\; w(\pm 1) \;=\; [\mathrm{D}v(\cdot)](\pm 1) \;=\; 0.
$$

In this representation the operator-valued matrix $\mathcal{A}$ is of size 4×4 with components

$$\mathcal{A}(i,j) = \left(\sum_{n=0}^{2} a_{n,ij}(y,\omega)\mathrm{D}^n \right),$$

where the nonzero coefficients $a_{n,ij}$ are given by

$$
\begin{aligned}
a_{2,11} &= -\frac{(1-\beta)}{We\,c(y)} - \beta,\\
a_{1,11} &= \frac{(1-\beta)\,\left(c'(y) - ik_x\,\left(3We\,c(y)\bar{T}_{xy}(y) + 2\bar{U}'(y)\right)\right)}{We\,c(y)^2},\\
a_{0,11} &= \frac{(1-\beta)\,k_x\,\bar{T}_{xy}(y)\left(2k_x\,\bar{U}'(y) + ic'(y)\right)}{c(y)^2}\\
&\quad + \frac{(1-\beta)\,\left(2k_x^2 + k_x\,We\,\left(2k_x\,\bar{T}_{xx}(y) - i\bar{T}'_{xy}(y)\right) + k_z^2\right)}{We\,c(y)} + \beta k^2,\\
a_{2,12} &= -\frac{(1-\beta)\,\left(We\,c(y)\bar{T}_{xy}(y) + 2\bar{U}'(y)\right)}{We\,c(y)^2},\\
a_{1,12} &= \frac{(1-\beta)\,\bar{T}_{xy}(y)c'(y)}{c(y)^2} + \frac{4(1-\beta)\,c'(y)\bar{U}'(y)}{We\,c(y)^3} - \frac{i(1-\beta)\,k_x\,\bar{T}_{xx}(y)}{c(y)}\\
&\quad - \frac{4i(1-\beta)\,k_x\,\bar{T}_{xy}(y)\bar{U}'(y)}{c(y)^2} - \frac{4i(1-\beta)\,k_x\,\bar{U}'(y)^2}{We\,c(y)^3} - \frac{i(1-\beta)\,k_x}{We\,c(y)}\\
&\quad - \frac{2(1-\beta)\,\bar{U}''(y)}{We\,c(y)^2},
\end{aligned}
$$

$$
\begin{aligned}
a_{0,12} &= \frac{i(1-\beta)\,k_x\,\bar{T}_{xx}(y)c'(y)}{c(y)^2} + \frac{4i(1-\beta)\,k_x\,\bar{T}_{xy}(y)c'(y)\bar{U}'(y)}{c(y)^3}\\
&\quad + \frac{i(1-\beta)\,k_x\,c'(y)}{We\,c(y)^2} - \frac{(1-\beta)\,c'(y)\bar{T}'_{xy}(y)}{c(y)^2}\\
&\quad + \frac{2(1-\beta)\,k_x^2\bar{T}_{xx}(y)\bar{U}'(y)}{c(y)^2} + \frac{4(1-\beta)\,k_x^2\bar{T}_{xy}(y)\bar{U}'(y)^2}{c(y)^3}\\
&\quad + \frac{2(1-\beta)\,k_x^2\bar{U}'(y)}{We\,c(y)^2}\\
&\quad - \frac{2i(1-\beta)\,k_x\,\bar{T}_{xy}(y)\bar{U}''(y)}{c(y)^2} + \frac{(1-\beta)\,k_z^2\bar{U}'(y)}{We\,c(y)^2},\\
a_{1,13} &= -\frac{i(1-\beta)\,k_z\left(We\,c(y)\bar{T}_{xy}(y) + \bar{U}'(y)\right)}{We\,c(y)^2},\\
a_{0,13} &= \frac{(1-\beta)\,k_x\,k_z\left(We\,c(y)\bar{T}_{xx}(y) + c(y) + We\,\bar{T}_{xy}(y)\bar{U}'(y)\right)}{We\,c(y)^2},\\
a_{0,14} &= ik_x,\\
a_{1,21} &= -\frac{i(1-\beta)\,k_x}{We\,c(y)},\\
a_{0,21} &= \frac{(1-\beta)\,k_x^2\bar{T}_{xy}(y)}{c(y)},\\
a_{2,22} &= -\frac{2(1-\beta)}{We\,c(y)} - \beta,\\
a_{1,22} &= \frac{2(1-\beta)\,c'(y)}{We\,c(y)^2} - \frac{3i(1-\beta)\,k_x\,\bar{T}_{xy}(y)}{c(y)} - \frac{2i(1-\beta)\,k_x\,\bar{U}'(y)}{We\,c(y)^2},\\
a_{0,22} &= \frac{2i(1-\beta)\,k_x\,\bar{T}_{xy}(y)c'(y)}{c(y)^2} + \frac{(1-\beta)\,k_x^2\bar{T}_{xx}(y)}{c(y)}\\
&\quad + \frac{2(1-\beta)\,k_x^2\bar{T}_{xy}(y)\bar{U}'(y)}{c(y)^2}\\
&\quad + \frac{(1-\beta)\,k_x^2}{We\,c(y)} - \frac{i(1-\beta)\,k_x\,\bar{T}'_{xy}(y)}{c(y)} + \frac{(1-\beta)\,k_z^2}{We\,c(y)} + \beta k^2,\\
a_{1,23} &= -\frac{i(1-\beta)\,k_z}{We\,c(y)},\\
a_{0,23} &= \frac{(1-\beta)\,k_x\,k_z\bar{T}_{xy}(y)}{c(y)},\\
a_{1,24} &= 1,
\end{aligned}
$$

$$
\begin{aligned}
a_{0,31} &= \frac{(1-\beta)\,k_x\,k_z}{We\,c(y)},\\
a_{1,32} &= -\frac{i(1-\beta)\,k_z}{We\,c(y)},\\
a_{0,32} &= \frac{(1-\beta)\,k_z\left(k_x\,\bar{U}'(y) + ic'(y)\right)}{We\,c(y)^2},
\end{aligned}
$$

$$
\begin{aligned}
a_{2,33} &= -\frac{(1-\beta)}{We\,c(y)} - \beta,\\
a_{1,33} &= \frac{(1-\beta)\,c'(y)}{We\,c(y)^2} - \frac{2i(1-\beta)\,k_x\,\bar{T}_{xy}(y)}{c(y)} - \frac{i(1-\beta)\,k_x\,\bar{U}'(y)}{We\,c(y)^2},\\
a_{0,33} &= \frac{i(1-\beta)\,k_x\,\bar{T}_{xy}(y)c'(y)}{c(y)^2} + \frac{(1-\beta)\,k_x^2\bar{T}_{xx}(y)}{c(y)} + \frac{(1-\beta)\,k_x^2\bar{T}_{xy}(y)\bar{U}'(y)}{c(y)^2}\\
&\quad + \frac{(1-\beta)\,k_x^2}{We\,c(y)} - \frac{i(1-\beta)\,k_x\,\bar{T}'_{xy}(y)}{c(y)} + \frac{2(1-\beta)\,k_z^2}{We\,c(y)} + \beta k^2,\\
a_{0,34} &= ik_z.
\end{aligned}
$$

The expressions for $\mathcal{B}$ and $\mathcal{C}_v$ are given by

$$\mathcal{B} = \begin{bmatrix} 1 & 0 & 0\\ 0 & 1 & 0\\ 0 & 0 & 1\\ 0 & 0 & 0 \end{bmatrix}, \qquad \mathcal{C}_v = \begin{bmatrix} 1 & 0 & 0 & 0\\ 0 & 1 & 0 & 0\\ 0 & 0 & 1 & 0 \end{bmatrix},$$

and for the stress output τ_{xx}, $\mathcal{C}_{xx}$ is a 1×4 block-matrix operator given by

$$\mathcal{C}_{xx}(i,j) = \left(\sum_{n=0}^{1} c_{n,ij}(y,\omega)\mathrm{D}^n \right), \tag{A.3}$$

where the nonzero coefficients $c_{n,ij}$ are given by

$$
\begin{aligned}
c_{1,11} &= \frac{2\left(We\,c(y)\bar{T}_{xy}(y) + \bar{U}'(y)\right)}{We\,c(y)^2},\\
c_{0,11} &= \frac{2ik_x\,\left(We\,c(y)\bar{T}_{xx}(y) + c(y) + We\,\bar{T}_{xy}(y)\bar{U}'(y)\right)}{We\,c(y)^2},\\
c_{1,12} &= \frac{2\bar{U}'(y)\left(We\,c(y)\bar{T}_{xy}(y) + 2\bar{U}'(y)\right)}{We\,c(y)^3},\\
c_{0,12} &= \frac{2i\bar{U}'(y)\left(k_x\,We\,\bar{T}_{xx}(y) + k_x + iWe\,\bar{T}'_{xy}(y)\right)}{We\,c(y)^2}\\
&\quad + \frac{-c(y)^2\bar{T}'_{xx}(y) + 4ik_x\,\bar{T}_{xy}(y)\bar{U}'(y)^2}{c(y)^3}.
\end{aligned}
\tag{A.4}
$$

Appendix B. Validation

In this section we present a few representative calculations that validate our numerical discretization presented in Section 3. Fig. B.1 shows calculations for 2D Couette flow with $\beta = 0.5$, $\omega = 0$, and $k_x = 1$ using three approaches: the ultraspherical method with the evolution form (see Appendix A.1), the spectral integration method with the descriptor form (see Appendix A.2), and the spectral integration method with the evolution form (see Appendix A.1) using 150 basis functions in each case. Fig. B.1a shows singular values of $\mathcal{T}_v$ in (14), and Fig. B.1b shows singular values of $\mathcal{T}_{xx}$ in (17). We find good agreement in the results obtained from the three approaches. Furthermore the singular values of $\mathcal{T}_v$ in Fig. B.1a agree quantitatively with the results of Lieu and Jovanović, Figure 8a in [32].

Next we plot the principal singular values from the SVD of $\mathcal{T}_v$ (14) and $\mathcal{T}_{xx}$ (17) for 2D3C Couette flow with $\beta = 0.5$, $k_z = 1$, and $\omega = 0$ in Fig. B.2. We present results that use the ultraspherical method, although we have confirmed that the spectral integration method (using both the descriptor and evolution forms) produces identical results. Fig. B.2a shows singular values of $\mathcal{T}_v$ in (14) as a function of We, and we observe that the singular values scale linearly with We (as indicated by the dashed line). Fig. B.2b shows singular values of $\mathcal{T}_{xx}$ in (17) scaling as We^2 on a log–log plot, as indicated by the dashed line. These scalings

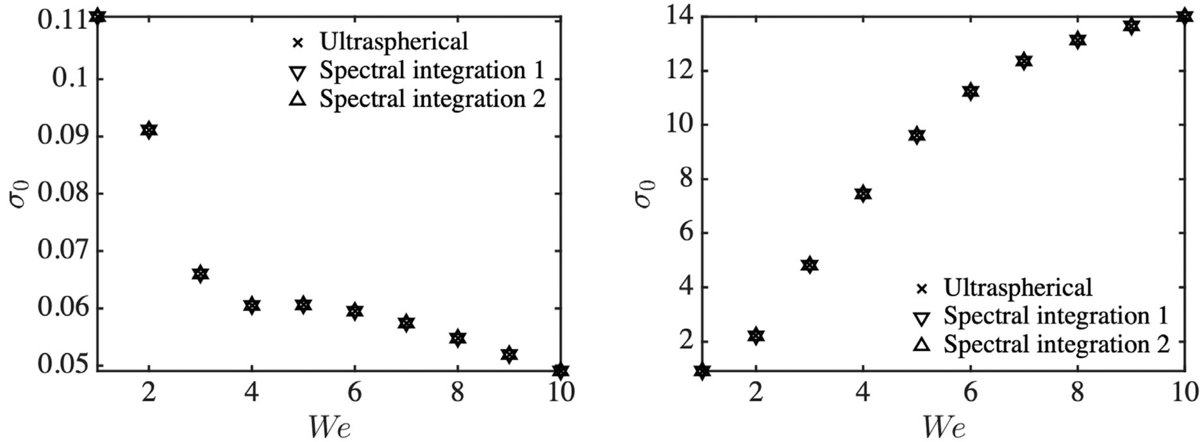

(a) $\boldsymbol{v}$ output (b) τ_{xx} output

Fig. B.1. Principal singular values of (a) $\mathcal{T}_v$ in (14) and (b) $\mathcal{T}_{xx}$ in (17) of 2D Couette flow of an Oldroyd-B fluid with $\beta = 0.5$, $k_x = 1$, and $\omega = 0$. Spectral integration 1 uses the descriptor form in Appendix A.2, and Spectral integration 2 uses the evolution form in Appendix A.1. The ultraspherical method uses the evolution form.

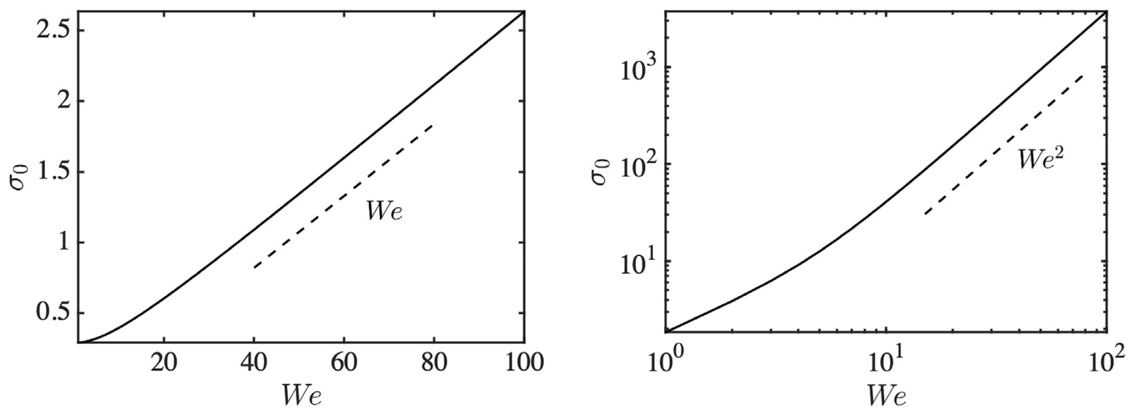

(a) $\boldsymbol{v}$ output (b) τ_{xx} output

Fig. B.2. Principal singular values of (a) $\mathcal{T}_v$ in (14) and (b) $\mathcal{T}_{xx}$ in (17) of 2D3C Couette flow of an Oldroyd-B fluid with $\beta = 0.5$, $k_z = 1$, and $\omega = 0$. The solid lines mark singular values, and the dashed lines show the slope of their scaling with We [15].

of the velocity and the stress singular values with We are in agreement with Figures 3 and 4 in [15].

References

[1] A. Groisman, V. Steinberg, Elastic turbulence in a polymer solution flow, Nature 405 (2000) 53–55.

[2] A. Groisman, V. Steinberg, Elastic turbulence in curvilinear flows of polymer solutions, New J. Phys. 6 (2004) 29.

[3] L. Pan, A.N. Morozov, C. Wagner, P.E. Arratia, Nonlinear elastic instability in channel flows at low Reynolds numbers, Phys. Rev. Lett. 110 (2013) 174502.

[4] B. Qin, P.E. Arratia, Characterizing elastic turbulence in channel flows at low Reynolds number, Phys. Rev. Fluids 2 (2017) 083302.

[5] T. Burghelea, E. Segre, I. Bar-Joseph, A. Groisman, V. Steinberg, Chaotic flow and efficient mixing in a microchannel with a polymer solution, Phys. Rev. E 69 (2004) 066305.

[6] S.G. Kandlikar, High flux heat removal with microchannels - A roadmap of challenges and opportunities, Heat Transfer Eng. 26 (2005) 5–14.

[7] R.G. Larson, Instabilities in viscoelastic flows, Rheol. Acta 31 (1992) 213–263.

[8] A.N. Morozov, W. van Saarloos, Subcritical finite-amplitude solutions for plane Couette flow of viscoelastic fluids, Phys. Rev. Lett. 95 (2005) 024501.

[9] M. Renardy, Y. Renardy, Linear stability of plane Couette flow of an upper convected Maxwell fluid, J. Non-Newton. Fluid Mech. 22 (1986) 23–33.

[10] V.A. Gorodtsov, A.I. Leonov, On a linear instability of a plane parallel Couette flow of viscoelastic fluid, J. Appl. Math. Mech. 31 (1967) 310–319.

[11] R. Sureshkumar, A.N. Beris, Linear stability analysis of viscoelastic Poiseuille flow using an Arnoldi-based orthogonalization algorithm, J. Non-Newton. Fluid Mech. 56 (1995) 151–182.

[12] N. Hoda, M.R. Jovanović, S. Kumar, Energy amplification in channel flows of viscoelastic fluids, J. Fluid Mech. 601 (2008) 407–424.

[13] N. Hoda, M.R. Jovanović, S. Kumar, Frequency responses of streamwise-constant perturbations in channel flows of Oldroyd-B fluids, J. Fluid Mech. 625 (2009) 411–434.

[14] M.R. Jovanović, S. Kumar, Transient growth without inertia, Phys. Fluids 22 (2010) 023101.

[15] M.R. Jovanović, S. Kumar, Nonmodal amplification of stochastic disturbances in strongly elastic channel flows, J. Non-Newton. Fluid Mech. 166 (2011) 755–778.

[16] B.K. Lieu, M.R. Jovanović, S. Kumar, Worst-case amplification of disturbances in inertialess Couette flow of viscoelastic fluids, J. Fluid Mech. 723 (2013) 232–263.

[17] G. Hariharan, M.R. Jovanović, S. Kumar, Amplification of localized body forces in channel flows of viscoelastic fluids, J. Non-Newton. Fluid Mech. 260 (2018) 40–53.

[18] M.R. Jovanović, From bypass transition to flow control and data-driven turbulence modeling: an input-output viewpoint, Annu. Rev. Fluid Mech. 53 (1) (2021) 311–345.

[19] M.R. Jovanović, B. Bamieh, Componentwise energy amplification in channel flows, J. Fluid Mech. 534 (2005) 145–183.

[20] B.F. Farrell, P.J. Ioannou, Stochastic forcing of the linearized Navier-Stokes equations, Phys. Fluids A 5 (1993) 2600–2609.

[21] P.J. Schmid, D.S. Henningson, Stability and Transition in Shear Flows, Springer Science and Business Media, 2012.

[22] B. Thomases, M. Shelley, Emergence of singular structures in Oldroyd-B fluids, Phys. Fluids 19 (2007) 103103.

[23] M. Grilli, A. Vázquez-Quesada, M. Ellero, Transition to turbulence and mixing in a viscoelastic fluid flowing inside a channel with a periodic array of cylindrical obstacles, Phys. Rev. Lett. 110 (2013) 174501.

[24] A. Shekar, R.M. McMullen, S.-N. Wang, B.J. McKeon, M.D. Graham, Critical-layer structures and mechanisms in elastoinertial turbulence, Phys. Rev. Lett. 122 (2019) 124503.
[25] A. Shekar, R.M. McMullen, B.J. McKeon, M.D. Graham, Self-sustained elastoinertial Tollmien-Schlichting waves, J. Fluid Mech. 897 (2020) A3.
[26] P. Huerre, Open shear flow instabilities, in: G.K. Batchelor, H.K. Moffatt, M.G. Worster (Eds.), Perspectives in Fluid Dynamics, Cambridge University Press, 2000, pp. 159–229, chapter 4.
[27] G.H. McKinley, R.C. Armstrong, R.A. Brown, The wake instability in viscoelastic flow past confined circular cylinders, Philos. Trans. R. Soc. A 344 (1993) 265–304.
[28] R.G. Larson, The Structure and Rheology of Complex Fluids, Oxford University Press, 1998.
[29] R.B. Bird, C.F. Curtiss, R.C. Armstrong, O. Hassager, Dynamics of Polymeric Liquids, Vol. 2, Kinetic Theory, John Wiley and Sons, 1987.
[30] M.R. Khorrami, M.R. Malik, R.L. Ash, Application of spectral collocation techniques to the stability of swirling flows, J. Comput. Phys. 81 (1989) 206–229.
[31] M. Renardy, Location of the continuous spectrum in complex flows of the UCM fluid, J. Non-Newton. Fluid Mech. 94 (2000) 75–85.
[32] B.K. Lieu, M.R. Jovanović, Computation of frequency responses for linear time-invariant PDEs on a compact interval, J. Comput. Phys. 250 (2013) 246–269.
[33] G.H. Golub, C.F. Van Loan, Matrix Computations, JHU Press, 2012.
[34] W.C. Reynolds, S.C. Kassinos, One-point modelling of rapidly deformed homogeneous turbulence, Proc. R. Soc. Lond. A Math. Phys. Sci. 451 (1995) 87–104.
[35] G. Hariharan, Transition to Elastic Turbulence in Channel Flows (Ph.D. thesis), University of Minnesota, 2020.
[36] G. Hariharan, S. Kumar, M.R. Jovanović, Well-conditioned ultraspherical and spectral integration methods for resolvent analysis of channel flows of Newtonian and viscoelastic fluids, J. Comput. Phys. (2021) doi:10.1016/j.jcp.2021.110241; also arXiv:2005.04493.
[37] C. Lanczos, Linear Differential Operators, Society for Industrial and Applied Mathematics, 1996.
[38] S. Boyd, V. Balakrishnan, P. Kabamba, A bisection method for computing the $\mathcal{H}_\infty$ norm of a transfer matrix and related problems, Math. Control Signals Systems 2 (1989) 207–219.
[39] K. Du, On well-conditioned spectral collocation and spectral methods by the integral reformulation, SIAM J. Sci. Comput. 38 (2016) A3247–A3263.
[40] L. Greengard, Spectral integration and two-point boundary value problems, SIAM J. Numer. Anal. 28 (1991) 1071–1080.
[41] S. Olver, A. Townsend, A fast and well-conditioned spectral method, SIAM Rev. 55 (2013) 462–489.
[42] J.P. Boyd, Chebyshev and Fourier Spectral Methods, Courier Corporation, 2001.
[43] T.A. Driscoll, N. Hale, L.N. Trefethen, Chebfun Guide, Pafnuty Publications, 2014.